Three-dimensional tsunami propagation simulations using an unstructured mesh finite element model

Yusuke Oishi,[1] Matthew D. Piggott,[2,3] Takuto Maeda,[4] Stephan C. Kramer,[2] Gareth S. Collins,[2] Hiroaki Tsushima,[5] and Takashi Furumura[4,6]

[1] Large-scale tsunami propagation simulations from the fault region to the coast are conducted using a three-dimensional (3-D) parallel unstructured mesh finite element code (Fluidity-ICOM). Unlike conventional 2-D approximation models, our tsunami model solves the full 3-D incompressible Navier-Stokes (NS) equations. The model is tested against analytical solutions to simple dispersive wave propagation problems. Comparisons of our 3-D NS model results with those from linear shallow water and linear dispersive wave models demonstrate that the 3-D NS model simulates the dispersion of very short wavelength components more accurately than the 2-D models. This improved accuracy is achieved using only a small number (three to five) of vertical layers in the mesh. The numerical error in the wave velocity compared with the linear wave theory is less than 3% up to $kH = 40$, where k is the wave number and H is the sea depth. The same 2-D and 3-D models are also used to simulate two earthquake-generated tsunamis off the coast of Japan: the 2004 off Kii peninsula and the 2011 off Tohoku tsunamis. The linear dispersive and NS models showed good agreement in the leading waves but differed especially in their near-source, short wavelength dispersive wave components. This is consistent with the results from earlier tests, suggesting that the 3-D NS simulations are more accurate. The computational performance on a parallel computer showed good scalability up to 512 cores. By using a combination of unstructured meshes and high-performance computers, highly accurate 3-D tsunami simulations can be conducted in a practical timescale.

1. Introduction

[2] Hydrodynamic simulations of tsunamis play an important role in tsunami disaster mitigation. Tsunami early warning systems are based on huge databases of simulation results, and tsunami hazard maps rely on simulation results with the source models estimated by analyzing the historic earthquake record.

[1]Fujitsu Laboratories of Europe Ltd., Hayes Park Central, Middlesex, Hayes, UK.
[2]Grantham Institute for Climate Change, Imperial College London, South Kensington Campus, London, UK.
[3]Applied Modelling and Computation Group, Department of Earth Science and Engineering, Imperial College London, South Kensington Campus, London, UK.
[4]Earthquake Research Institute, University of Tokyo, Bunkyo-ku, Tokyo, Japan.
[5]Meteorological Research Institute, Japan Meteorological Agency, Tsukuba, Ibaraki, Japan.
[6]Center for Integrated Disaster Information Research, Interfaculty Initiative in Information Studies, University of Tokyo, Bunkyo-ku, Tokyo, Japan.

Corresponding author: Y. Oishi, Fujitsu Laboratories of Europe Ltd., Hayes Park Central, Hayes End Road, Hayes, Middlesex, UB4 8FE, UK. (Yusuke.Oishi@uk.fujitsu.com)

[3] In these simulations, a cost-effective 2-D model rather than a full 3-D simulation is usually applied in which 2-D equations of different approximation levels are employed in accordance with the temporal and spatial scales of the problem. For example, a 2-D linear long wave (shallow water) theory, which assumes the wavelength of the disturbance is large in comparison to the depth of the ocean, is often employed for offshore tsunami propagation in large domains that include the wave source region. The nonlinear version of this theory is often used for a shallow ocean or for modeling tsunami inundation in more restricted domains. When the treatment of the properties of wave dispersion is important in tsunami propagation and inundation, linear and nonlinear dispersive wave equations are used [e.g., *Peregrine*, 1967].

[4] Although conventional 2-D wave equations mentioned above are well studied and effectively predict tsunamis [e.g., *Tanioka et al.*, 1995], consideration of the 3-D equations, which involve less approximation, is necessary to achieve more accurate results. The 3-D Navier-Stokes (NS) equations have been applied in tsunami simulations; however, substantial computational costs restrict the scale of simulation area. They are generally capable of solving only for small domains, e.g., around a costal structure [e.g., *Xiao and Huang*, 2008] or to deal with a local tsunami generation

caused by landslides [e.g., *Abadie et al.*, 2010]. More widespread use of the 3-D NS equations in tsunami simulation clearly requires improvements in model efficiency.

[5] Fortunately, recent progress in the development of massively parallel supercomputers allows the solution of these computationally demanding 3-D equations in large domains, from the tsunami source region to the coast, within a practical time frame. For instance, *Saito and Furumura* [2009a] simulated an offshore tsunami using a 3-D model. One approach to improve 3-D NS model efficiency is to exploit such advances in computer power. Another, complementary approach is to use nonuniform spatial resolution. Conventional 2-D or more recent 3-D simulations [e.g., *Saito and Furumura*, 2009a] generally employ a finite difference method with structured (grid-like) meshes. However, unstructured meshes are perhaps more appropriate for tsunami simulation since they enable the accurate and efficient representation of complex coastlines and bathymetry due to their flexibility and their multiscale resolution capabilities. Indeed, to solve 2-D equations, some prior offshore tsunami simulations employ unstructured meshes with finite element or finite volume methods [e.g., *Castro et al.*, 2009; *Myers and Baptista*, 1995; *Kawahara et al.*, 1988; *Walters*, 2005; *Mitsotakis*, 2009; *Guesmia et al.*, 1998].

[6] In this paper, we describe and test a 3-D, parallel NS model for tsunami simulation that employs multiscale unstructured meshes. The simulation code is Fluidity-ICOM, a multipurpose finite element/control volume-based computational fluid dynamics and ocean dynamics code developed by Imperial College London and collaborators [*Piggott et al.*, 2008]. The governing equations and the discretization method are described in section 2. In sections 3.1 and 3.2, the model is verified through the use of test problems with analytical solutions. These results are also compared to the results from other conventional wave models. Finally, real-world case studies are considered in sections 4.1 and 4.2 for the tsunamis resulting from two earthquakes off the coast of Japan: the off Kii peninsula earthquake of 2004 and the off Tohoku earthquake of 2011. In particular, the present 3-D model is likely to be suitable to simulate the recent devastating tsunami in the off Tohoku area because of the complexity of the coastline in this area and the short wavelength waves generated by a large fault slip near the trench [e.g., *Maeda et al.*, 2011].

2. Computational Model

2.1. Incompressible 3-D Navier-Stokes Equation

[7] In this study, we model tsunami propagation using the incompressible 3-D NS equations

$$\frac{\partial \mathbf{u}}{\partial t} + \mathbf{u} \cdot \nabla \mathbf{u} + \nabla \frac{\bar{p}}{\rho_0} - v \nabla^2 \mathbf{u} + \mathbf{g} = 0, \qquad (1)$$

$$\nabla \cdot \mathbf{u} = 0, \qquad (2)$$

where $\mathbf{u}$ is velocity, $\bar{p}$ is pressure, ρ_0 is density, v (e. g., $= 10^{-6}$ m^{2}s^{-1}) is kinematic viscosity, and $\mathbf{g} = (0, 0, g)^T$ is the gravitational acceleration with $g = 9.81$ ms^{-2}. In the present model, a Coriolis force is omitted as we deal with near-field tsunamis.

[8] The pressure is divided into a hydrostatic pressure field—$\rho_0 gz$ and a perturbation p

$$\bar{p} = p - \rho_0 gz. \qquad (3)$$

[9] Substituting (3) into (1), the momentum equation takes the form

$$\frac{\partial \mathbf{u}}{\partial t} + \mathbf{u} \cdot \nabla \mathbf{u} + \nabla \frac{p}{\rho_0} - v \nabla^2 \mathbf{u} = 0. \qquad (4)$$

[10] The kinematic boundary condition is given at the free surface $z = \eta$

$$\frac{\partial \eta}{\partial t} = \left(-\frac{\partial \eta}{\partial x}, -\frac{\partial \eta}{\partial y}, 1 \right)^T \cdot \mathbf{u} = \frac{\mathbf{n}_{fs} \cdot \mathbf{u}}{\mathbf{n}_{fs} \cdot \mathbf{e_z}}, \qquad (5)$$

where $\mathbf{n}_{fs} = \left(-\frac{\partial \eta}{\partial x}, -\frac{\partial \eta}{\partial y}, 1 \right)^T / \left| \left(-\frac{\partial \eta}{\partial x}, -\frac{\partial \eta}{\partial y}, 1 \right)^T \right|$ and $\mathbf{e_z} = (0,0,1)^T$. At the free surface, the pressure $\bar{p}$ ($= p - \rho_0 gz$) is assumed to be zero, i.e., $p = \rho_0 g\eta$. With this and equation (5), we have the free surface boundary condition for pressure perturbation

$$\frac{\partial p}{\partial t} = \rho_0 g \frac{\partial \eta}{\partial t} = \rho_0 g \frac{\mathbf{n}_{fs} \cdot \mathbf{u}}{\mathbf{n}_{fs} \cdot \mathbf{e_z}}. \qquad (6)$$

[11] A no-normal flow boundary condition and a free-slip boundary condition are applied at the bottom of the ocean and on coastlines

$$\mathbf{u} \cdot \mathbf{n}_b = 0, \frac{\partial \mathbf{u} \cdot \mathbf{t}_k}{\partial n} = 0, \qquad (7)$$

where $\mathbf{n}_b$ is the unit vector parallel to the normal, $\mathbf{t}_k$ ($k = 1,2$) form an orthogonal set of unit tangential vectors at the sea bottom, respectively, and n is the direction normal to the sea bottom. With a free-slip condition, a boundary layer at the sea bottom is avoided, which enables a small number of vertical layers (e.g., three or five layers) to accurately simulate wave propagation. A comparison between free-slip and no-slip conditions is discussed in section D. The number of vertical layers of nodes is such that velocity and pressure profiles in the vertical direction are sufficiently resolved as discussed in section 3. Hereafter, we call the number of layers of nodes "layers". Three and five layers have two and four elements in the vertical direction. The ocean bottom friction is also not considered here since it is known that such friction is of minimal importance for tsunami propagation in a deep ocean, and this has been verified for the present model.

[12] For the noncoastal boundaries, a sponge buffer zone is created surrounding the simulation region in order to suppress artificial reflections [e.g., *Cerjan et al.*, 1985]. In the sponge buffer zone, an absorption term $-\sigma \mathbf{u}$ is added to the right-hand side of the momentum equations, where σ is the coefficient for the absorption. The magnitude of the coefficient is increased with distance into the sponge, with the outer most part having the largest value of 0.01 s^{-1}.

[13] In this paper, an initial condition is given as a free surface elevation, which is imposed as a pressure perturbation p ($= \rho_0 g\eta$) in the simulation. Dynamical sea bottom deformation can also be simulated by the present model employing a vertical inflow boundary condition for velocity, which
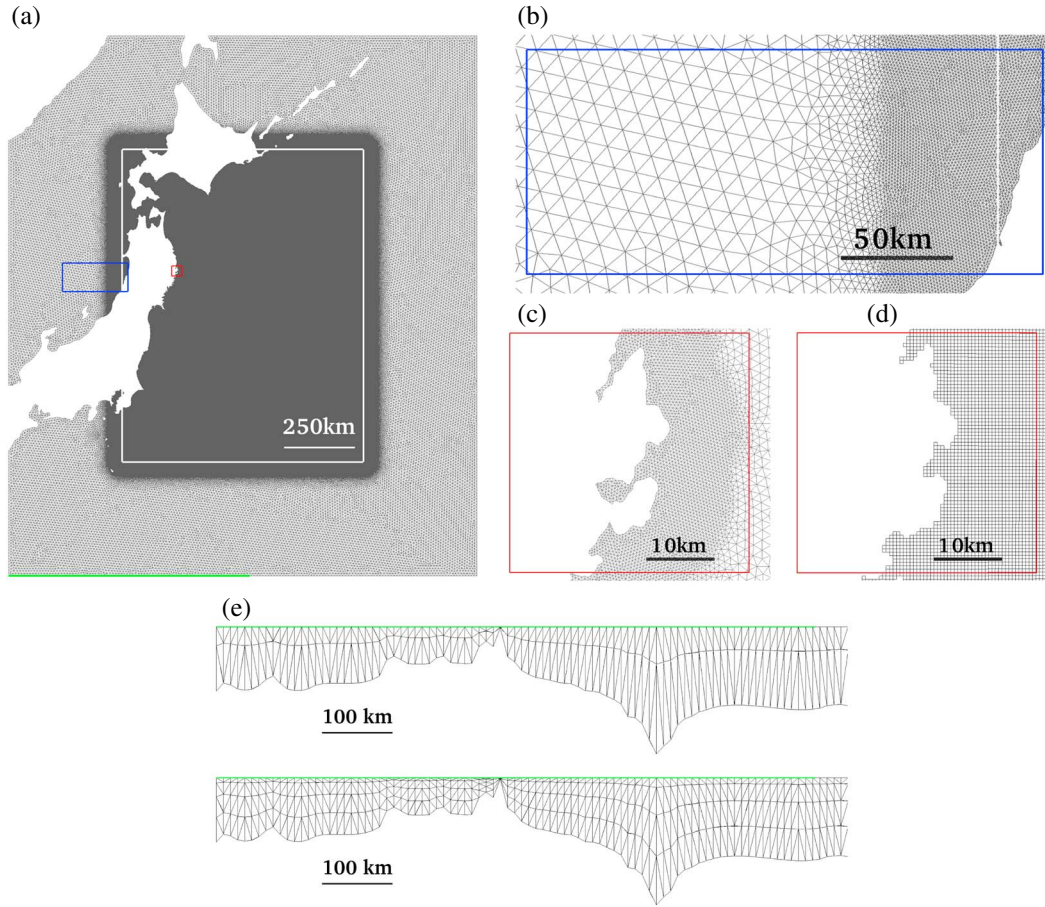
Figure 1. (a) Unstructured horizontal mesh used for the simulations on the off Tohoku earthquake tsunami in the NS model. The mesh spacing ranges from 500 m to 10 km. The domain outside the white square is a sponge region. Ninety-four percent of the mesh nodes are located either inside the white square or within 50 km of it. (b) Close-up of Figure 1a. The blue square shown in the figure is same size and position as the blue square in Figure 1a. (c) Close-up of Figure 1a. The red square shown in the figure is the same as the red square in Figure 1a. (d) The structured orthogonal mesh. The resolution is 500 m everywhere. The red square shown in the figure is same size and position as the red squares in Figures 1a and 1c. (e) Lateral faces of the 3-D meshes with three and five nonuniform vertical layers. The green line in Figure 1e corresponds to the green line in Figure 1a. The mesh is extended in the vertical direction by a factor of 20 for illustration purposes.

corresponds to the movement of seawater just above the sea bottom [*Saito and Furumura*, 2009a, 2009b]. Such simulations will be reported in future work.

2.2. Spatial and Temporal Discretizations

[14] In this section, the essentials of the spatial and temporal discretizations and the unstructured simulation meshes are illustrated. More details of the discretization can be found in section A.

[15] In the present model, the spatial discretization uses the Galerkin finite element method based on a mixed discontinuous/continuous element pair, with continuous quadratic pressure and discontinuous linear velocity. This so-called $P_{1,DG}P_2$ approach was developed for the accurate representation of geostrophic balance while satisfying the Ladyshenskaja-Babuška-Brezzi (LBB) stability condition [*Cotter et al.*, 2009a, 2009b] and is now implemented in Fluidity-ICOM. Although a Coriolis force is omitted in the present model, the stability and increased order of accuracy of the method are helpful to achieve accurate results.

[16] With this element pair, pressure has three degrees of freedom (DOF) per element edge and velocity has two. However, taking into account the discontinuity of velocity between elements, the DOF count for velocity is usually larger than that of pressure. Also, it is to be noted that both velocity and pressure have larger DOF counts than the number of mesh nodes, due to the use of discontinuous linear functions for velocity and continuous quadratic functions for pressure.

[17] For the temporal integration, the Crank-Nicolson scheme is employed, which yields second-order temporal accuracy. To satisfy the continuity equation, we use a pressure correction method [e.g., *Gresho et al.*, 1984]. A discrete Poisson equation needs to be solved at each time step.

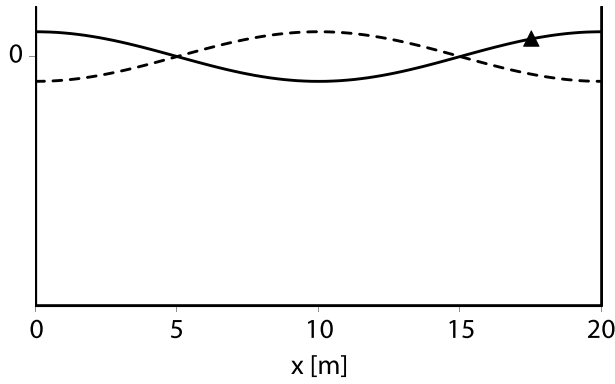[18] A 2-D horizontal unstructured triangular mesh at the sea surface is generated using Gmsh with the frontal

Figure 2. Standing wave in a closed basin. The width of the domain is fixed to 20 m and its depth H is chosen from 1, 8, 16, 32, 64, 96, or 128 m. The wave height is always $H/100$. Triangle is at $x = 17.5$ m, where the wave height is measured.

algorithm (http://geuz.org/gmsh/), and it is perpendicularly extruded down to the sea bottom resulting in a tetrahedral mesh in 3-D. In the case of two vertical layers (of nodes), the nodes are positioned at the sea surface and the seafloor. When more than three vertical layers are employed, the vertical positions of the nodes are defined, depending on the local depth, and the number of the vertical layers is kept constant everywhere except for very shallow regions. In the vertical direction, the nodes can be uniformly or nonuniformly distributed. To reproduce the hyperbolic profiles of the variables of the waves which are far from the long wave limit, the nodes are positioned nonuniformly at $z = H \sin(j\pi/2(N-1))$ for $1 \leq j \leq N$ in the N vertical layers case.

[19] An example of a horizontal mesh for the off Tohoku region used in section 4.2 is shown in Figure 1a, and the unstructured mesh is compared to an orthogonal structured mesh which is often used in 2-D models. It can be seen that the unstructured mesh reproduces the complicated coastline more precisely than the structured mesh of the same level of resolution. The unstructured mesh is concentrated around the Sanriku coast with a length scale of approximately 500 m, and the resolution is gradually reduced moving to the open ocean with length scales of approximately 1.5 km (Figure 1c). In this model, the resolution of the outer edge of the sponge region is approximately 10 km (Figure 1b).
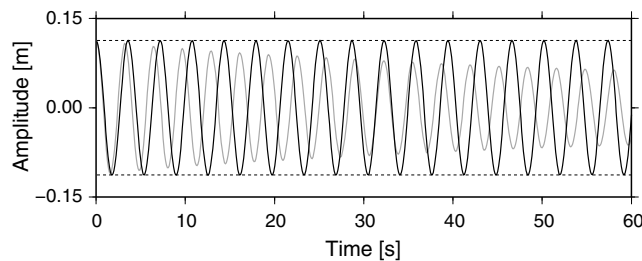

Figure 3. The time series of the amplitude of standing wave in a closed basin at $x = 17.5$ m. Black line indicates the result from the model with the nonuniform vertical meshes with five layers (of nodes), gray line from two vertical layers.

This relatively large value is chosen in order to reduce the computation overhead of the sponge region, which is permissible since we are not particularly interested in the solution behavior there. The lateral faces of the southern edge of the 3-D meshes for the cases with three and five nonuniform vertical layers are shown in Figure 1e. In both meshes, the number of vertical layers is two in the regions shallower than 50 m. In section 4.2, three vertical layers were employed. On the other hand, for the 2004 off Kii peninsula tsunami case in section 4.1, five vertical layers were used.

3. Numerical Tests

[20] To understand the effectiveness of the present 3-D NS simulation compared with conventional 2-D models for simulations of tsunami and to understand the basic characteristics of simulated tsunami derived by each model in detail, two kinds of comparisons to analytical solutions were conducted: a standing wave in a closed basin and wave dispersion in an ocean of constant depth.
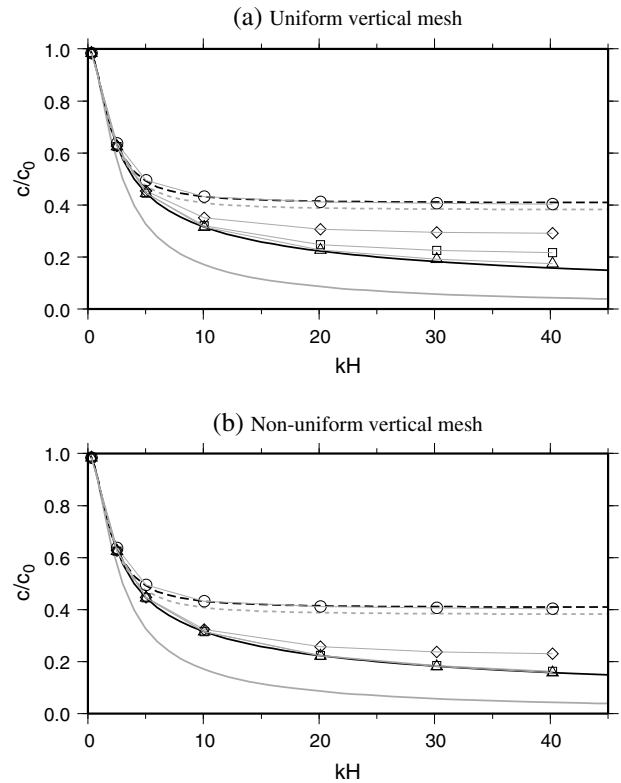

Figure 4. Dispersion relations for the linear wave theory, NS model, and dispersive wave models. Black line denotes the solution from the linear wave theories, black dotted line is the theoretical solution of the dispersive wave equations that has the dispersion relation of equation (10) with $\alpha = -0.4$, gray dotted line is the dispersive wave equations that has the relation of equation (10) with $\alpha = -0.39$, and gray solid line is the dispersive wave equations categorized in the dispersive relation of equation (9). The NS model with two layers (of nodes) is shown as circles, three layers diamonds, five layers squares, and nine layers triangles.
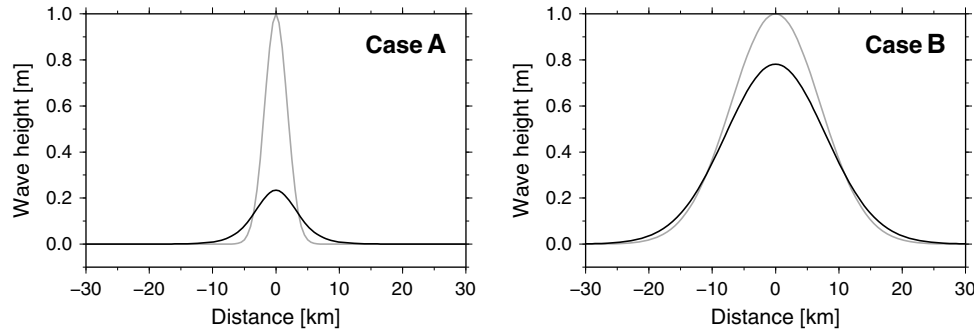
Figure 5. Initial surface deformation (black lines) calculated from the given bottom deformation (gray lines) in the *xz* plane for Case A and Case B.

3.1. Standing Wave in Closed Basin

[21] The standing wave in a closed basin of constant depth was calculated to assess the discrete dispersive relation of the present model [e.g., *Walters*, 2005; *Ai et al.*, 2010]. The initial wave height that causes a standing wave with a wavelength λ was given as $\eta = A\cos(2\pi x/\lambda)$ at $t=0$ where A is the amplitude. The width of the basin was chosen to be the same as the wavelength λ. In all the simulations, λ was fixed as 20 m, and the depth of the basin H was varied. A was always set to $H/100$. The wave height at $x=17.5$ m was measured. The model setup is illustrated in Figure 2.

[22] For this example, the NS model was employed in 2-D vertical slice geometry; the vertical plane was solved with the same equations and discretization as the present 3-D model. The horizontal 1-D meshes were structured and had 1 m spacing and the time step was 0.1 s. In the vertical direction, we tested uniform and nonuniform meshes. In the nonuniform meshes, nodes were gathered near the surface to efficiently reproduce the vertical structure of pressure and velocity of short wavelength waves, which have the shape of a hyperbolic function in the vertical direction.
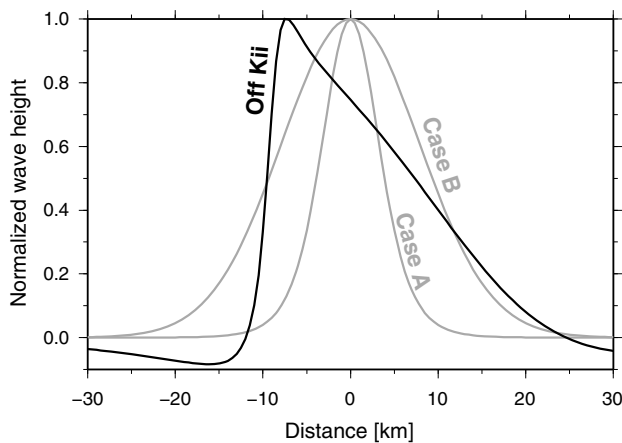
[23] Linear wave theory describes the linear dispersive relation of the wave as

$$\frac{c}{c_0} = \sqrt{\frac{1}{kH}\tanh kH},\qquad(8)$$

where $k=2\pi/\lambda$ is the wave number, c is the wave velocity, and $c_0 = \sqrt{gH}$. When $H=16$ m and $kH=5.02$, c/c_0 is 0.446. For the case of $H=16$ m, the measurements at

Figure 6. The shapes of the surface deformations for the test cases in Figure 5 are compared to the initial wave height of the off Kii peninsula earthquake case. The heights are normalized by the maximum values.
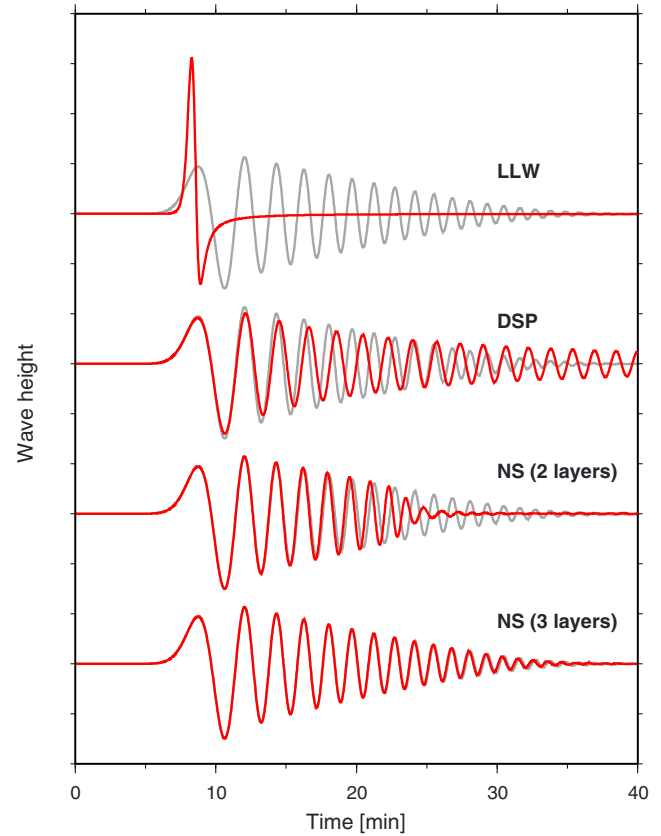

Figure 7. Waveforms of Case A at the point 100 km from the source are shown. Vertical axis is the wave height with tick marks at every 0.01 m. The gray lines are the analytical solution, and the red lines are the simulation results. In the NS model with three layers, nonuniform vertical mesh is employed.
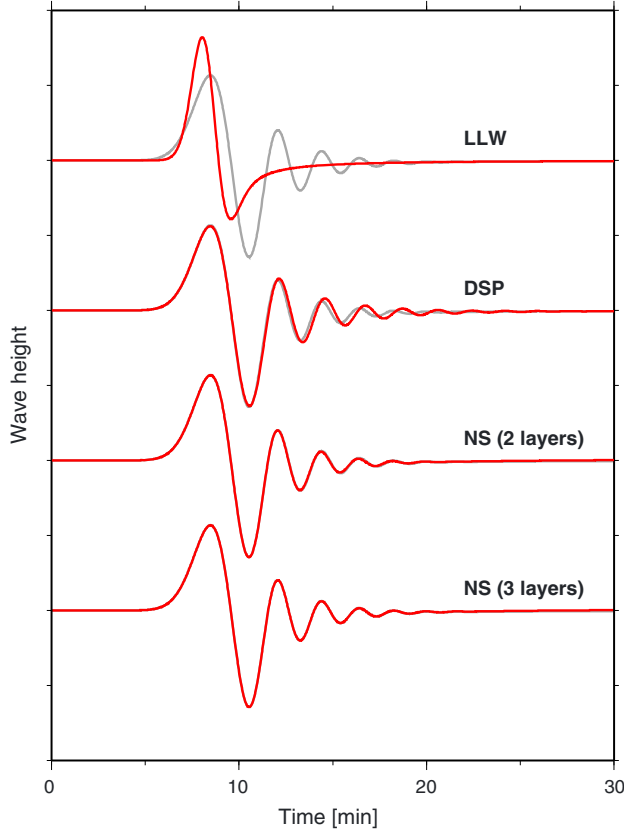
Figure 8. Same as Figure 7, but for Case B.

$x = 17.5$ m are shown in Figure 3. We can calculate c/c_0 as 0.495 for the two vertical layers (of nodes) case and 0.445 for the nonuniform five vertical layers case. When the vertical resolution is not sufficient, the wave velocity tends to be faster than the analytical solution, and the wave amplitude tends to be smaller.

[24] The calculated dispersive relations compared with that from linear wave theory are shown in Figure 4. From this analysis, it is evident that the nonuniform grid efficiently improves accuracy and five vertical layers are enough to reproduce the correct wave velocity within 3% error up to $kH = 40$. The nonuniform vertical grid with five layers showed about 10 times better accuracy than the corresponding uniform grid with the same number of layers.

[25] For comparison, the linear dispersive relations of the dispersive wave model employed in the following sections, and the relations of other representative models are considered here. The dispersive wave model (details in section B) employed in the following sections has the linear dispersive relation of

$$\frac{c}{c_0} = \sqrt{\frac{1}{1 + (kH)^2/3}}, \tag{9}$$

which can be obtained by assuming a sinusoidal wave $A \exp i$ $(kx - \omega t)$, where ω is angular frequency and A is amplitude. The equations of *Peregrine* [1967] have the same dispersive relation as equation (9). The dispersion relation of the equations by *Nwogu* [1993], *Madsen and Sørensen* [1992], and *Beji and Nadaoka* [1996] can be written as

$$\frac{c}{c_0} = \sqrt{\frac{1 - (\alpha + 1/3)(kH)^2}{1 - \alpha(kH)^2}}, \tag{10}$$

which changes depending on the value of α. *Beji and Nadaoka* [1996] and *Madsen and Sørensen* [1992] employed $\alpha = -0.4$, whereas *Nwogu* [1993] showed that $\alpha = -0.39$ results in a dispersion relation with less error. The relation of equations (9) and (10) with $\alpha = -0.39$ and equation (10) with $\alpha = -0.4$ are plotted in Figure 4. When kH is large, the dispersive wave theory model employed here has a dispersive relation that predicts a smaller wave velocity than that of the analytical solution; the dispersive effect is overestimated.

[26] The NS model with the lowest possible vertical resolution (two layers of nodes) shows almost the same dispersive relation as equation (10) with $\alpha = -0.4$, which
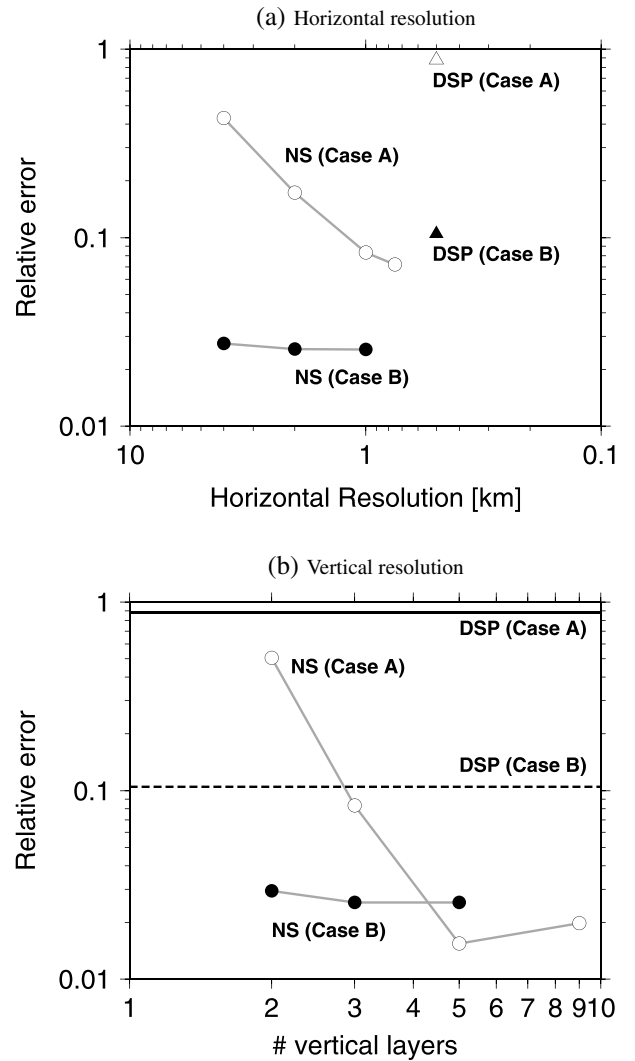

Figure 9. Convergence of relative error norms between the analytical solutions and the simulations with different resolutions. The error is calculated from the waveforms in Figures 6 and 7 from $t = 0$ to 40 min. (a) Varying the horizontal resolution. (b) Varying the number of vertical layers (of nodes). In the NS models with more than three layers, a nonuniform vertical mesh is employed.
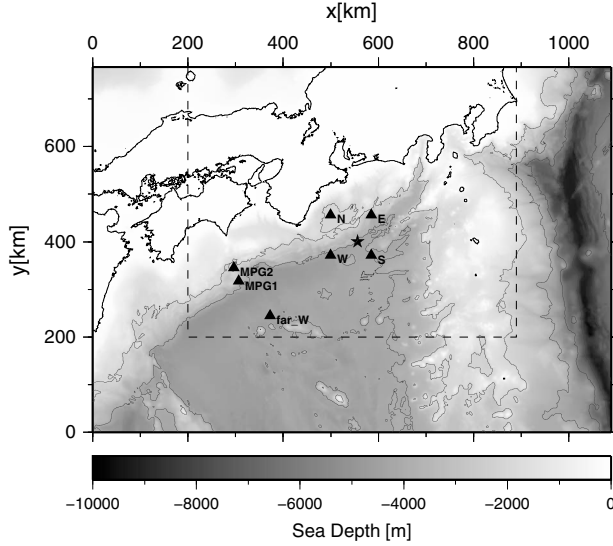
Figure 10. Bathymetry around Kii Peninsula, Japan. The locations of the ocean bottom pressure gauges are shown as MPG1 and MPG2. The simulated waveforms are also examined at N, E, S, W, and far W. The region outside the smaller dotted line square is used as a sponge region to prevent artificial reflections at the open boundary. The epicenter at (137.14°E, 33.14°N) is shown by a solid star. The contour lines of the bathymetry at $H = -2000$ m and -4000 m are also shown.

converges to $\sqrt{1/6}$ when kH is large. The relation of the equation (10) with $\alpha = -0.39$ is slightly better than that with $\alpha = -0.4$. When more than two vertical layers are used, the NS model always shows better results than all the dispersive wave models compared here.

[27] When $H = 5000$ m, $kH = 40$ corresponds to a wavelength of 785 m, which is similar to the typical horizontal resolution of tsunami propagation simulations. The ocean off the east coast of Japan can have depths of 5000 m within a few hundred kilometers from the coast, so a dispersive wave model accurate up to $kH > O(10)$ may be useful for simulating tsunami propagation around Japan.

3.2. Wave Dispersion

[28] In this section, we compare wave propagation in a 3-D domain with a constant depth between the models based on the linear long wave (LLW) equations, the linear dispersive wave (DSP) equations, and the NS equations. This constant depth case has an analytical solution [e.g., *Takahashi*, 1942], which provides the time series of the sea surface deformation (wave generation and propagation phases) corresponding to the given sea bottom deformation. The details of the linear wave models and the analytical solution are described in sections B and C, respectively. In each model, the sea depth was given as $H = 4000$ m. The horizontal resolution for the LLW and DSP models was 500 m. In the NS model, the length scale for the horizontal mesh spacing was $L_c = 1$ km, and nonuniform vertical meshes with five layers (of nodes) were employed. The time step for every model was 1.0 s.

[29] The sea bottom deformation was prescribed by

$$d(x, y, t = 0) = d_0 \exp\left(\frac{-x^2 - y^2}{a^2}\right), \qquad (11)$$

with a characteristic length scale $a = 2.5$ km (Case A) and $a = 10$ km (Case B), which are shown with the corresponding analytical solutions for sea surface deformation in Figure 5. The amplitude of the sea surface deformation given by the analytical solution is smaller than the amplitude of the seafloor deformation because of the damping effect of the sea thickness. The sea surface deformation of the analytical solution, which assumes the deformation occurs instantaneously and is calculated by equation (C1), was used as the initial condition in the simulations, and the simulation results were compared to the wave propagation of the analytical solution.

[30] Figure 6 compares the shape of the initial wave height for the 2004 off Kii peninsula earthquake tsunami, which is tested in section 4.1, to the initial wave heights employed here. For the off Kii peninsula tsunami case, the wave height in the slice line perpendicular to the strike direction that goes over the point of maximum height is shown in Figure 6. Some parts of the source region of the off Kii peninsula earthquake had the similar sea depth to the present test cases (i.e., $H = 4000$ m), and so the actual tsunami waves in the same depth ocean may consist of both shorter- and longer-wavelength components compared with the waves tested here.

[31] The wave heights at $x = 100$ km and $y = 0$ km are plotted for each model as a function of time in Figure 7 (Case A) and Figure 8 (Case B). In both cases, the DSP and NS models produce wave dispersion, whereas the LLW model does not. In the LLW model, the first wave peak arrives sooner and has greater amplitude than the analytical solution.

[32] In Case B (Figure 8), the amplitude and arrival time and the first wave peak predicted by the DSP model is almost the same as the analytical solution, but the wave velocity of the
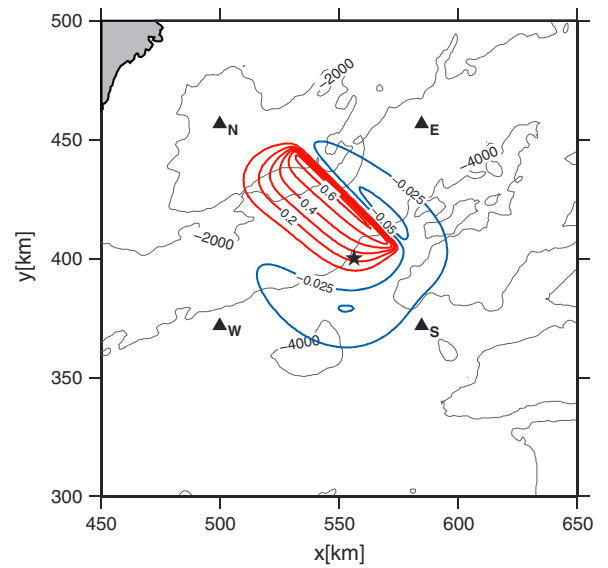

Figure 11. Initial water height for the simulation of the off Kii peninsula earthquake tsunami is shown by red contour lines which range from 0.1 to 0.6 m with step size of 0.1 m and blue contour lines which range from -0.05 to -0.025 m with step size of 0.025 m. The contour lines of the bathymetry at $H = -2000$ and -4000 m are also shown.

(a) Linear long wave model

(b) Linear dispersive wave model
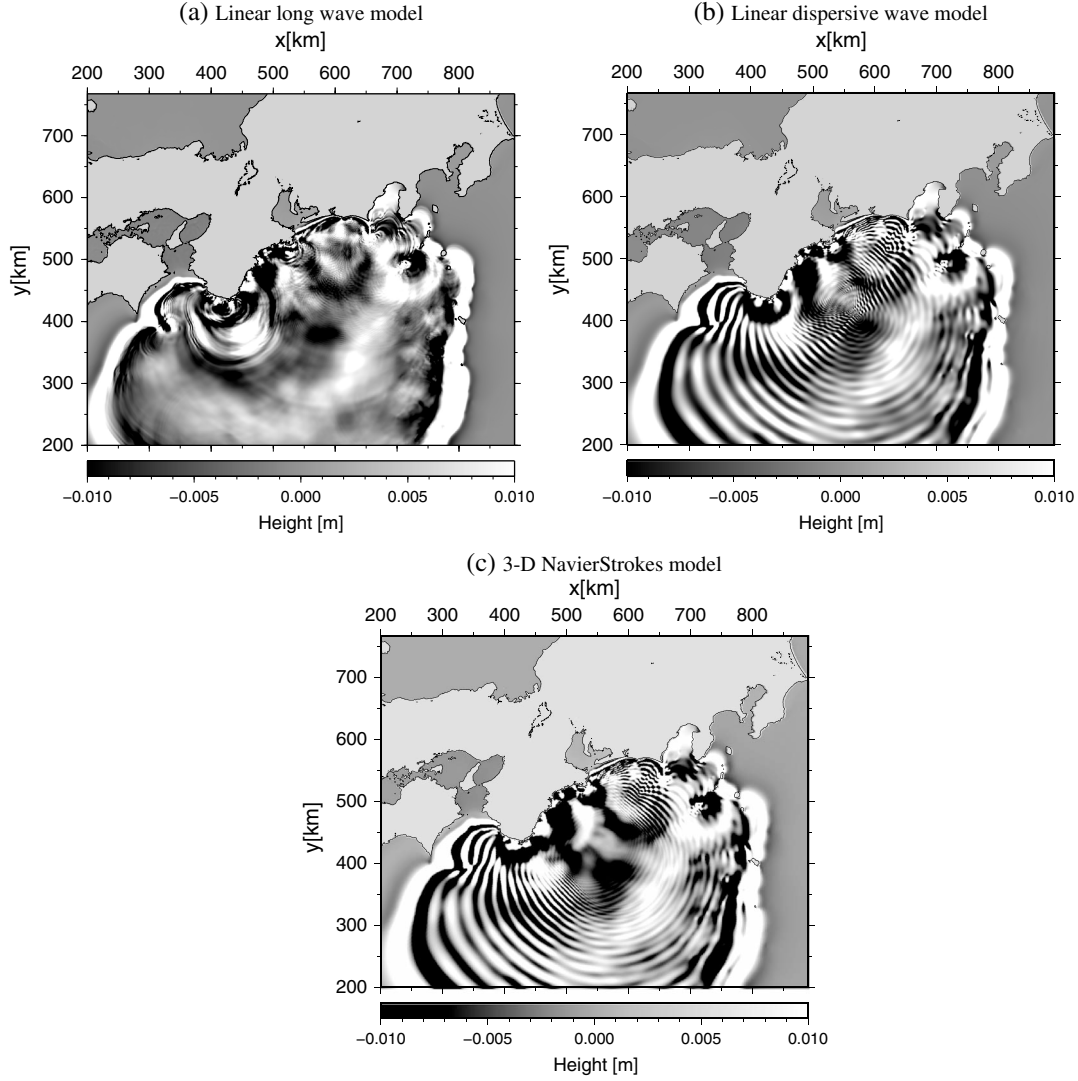
(c) 3-D NavierStrokes model

Figure 12. Snapshots at 30 min of the simulations of the off Kii peninsula earthquake tsunami of 2004. In the NS model, five nonuniform vertical layers (of nodes) are employed. Only the domain excluding the sponge region of the NS model is shown.

dispersive waves is slightly lower than the analytical solution. This is consistent with the dispersive relation obtained in the previous section. The NS models with two and three nonuniform vertical layers agree very well with the analytical solution.

[33] In Case A (Figure 7), the discrepancy between the DSP model and the analytical solution is more obvious. The dispersive waves are delayed considerably, and spurious waves remain around the source region. Only the initial peak shows good agreement. In this case, the NS model with two vertical layers does not match the analytical solution either. The dispersive waves show good agreement until around 20 min; after this time, they arrive earlier than predicted by the analytical solution and then disappear at around 25 min. This is because the wave velocity of this model cannot be slower than around $\sqrt{1/6}$ c_0 as discussed in section 3.1. The dispersive models that have the same dispersive relation as the NS model with two layers would show the same tendency.

[34] In Case A, the NS model with three vertical layers agrees very well with the analytical solution, showing the

advantage of the NS model in reproducing short wavelength waves. From these results, it is evident that the NS model correctly represents the dispersion characteristics of even short wavelength waves, whereas the 2-D models are only accurate for longer wavelength components. When short wavelength waves are important, the increased vertical resolution of the NS model is essential.

[35] The sensitivity of the NS model results to changes in vertical and horizontal resolution is shown in Figure 9. The relative error norm shown in these plots is defined as

$$\text{relative error} = \sqrt{\frac{\sum_{n=0}^{Nt} \left(\eta^n_{\text{model}} - \eta^n_{\text{analytical}} \right)^2}{\sum_{n=0}^{Nt} \left(\eta^n_{\text{analytical}} \right)^2}}, \quad (12)$$

where the superscript n refers to the time step index (with $\Delta t = 1$ s and N_t equal to 40 min). This relative error was
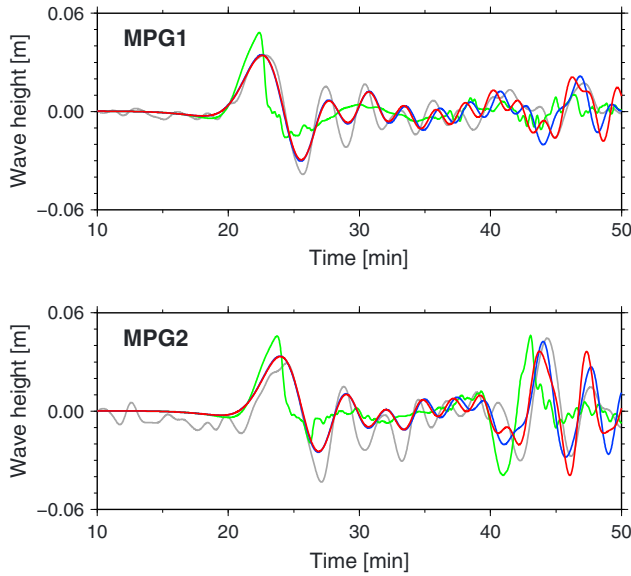
Figure 13. Waveforms of 2004 off Kii peninsula earthquake tsunami at MPG1 and MPG2. Gray lines are the observation, red lines are the results from the NS model, blue lines are from the DSP model, and the green lines are from the LLW model.

measured for the waveforms in Figures 6 and 7. For the horizontal resolution test, the number of the vertical layers was fixed to three (Figure 9a); for the vertical resolution test, the horizontal resolution was fixed to $L_c = 1$ km (Figure 9b).

[36] Here we use the relative error of 0.1 as a reference point of acceptable error, which roughly corresponds to the Case B DSP model (Figure 8) or the Case A NS model with three layers (Figure 7). In terms of the horizontal resolution, a node separation of 4 km gives an acceptable error for Case B, and the error is not improved much by increasing the horizontal resolution. For Case A, the error converges to a minimum for a horizontal node separation of 750 m, but 1 km is enough to make the error less than 0.1. More discussion on the effect of horizontal resolution can be found in section E. In terms of the vertical resolution, two layers give a relative error less than 0.1 for Case B. For Case A, the error converges to a minimum when five layers are used, but three layers are sufficient to achieve a relative error less than 0.1. Although the error with nine layers seems to be a little larger compared to that of the five-layer case, both are negligibly small. Note that for Case A, the error of the DSP model is always larger than that of the NS model.

[37] Model sensitivity to time resolution was also tested and found to be negligible for time steps between 0.5 and 1.0 s.

4. 3-D NS Simulation of Tsunami From Recent Large Earthquakes

4.1. 2004 Off Kii Peninsula (M_w 7.4) Earthquake

[38] To compare the present 3-D NS model, LLW model and DSP model in a realistic setting, we used each model to simulate the tsunami caused by the off Kii Peninsula earthquake (M_w 7.4) of 5 September 2004. This offshore earthquake occurred inside the Philippine Sea plate, and the

Japan Metrological Agency estimated the depth of hypocenter as 44 km. Such a shallow, intraplate earthquake, which is often referred to as an outer-rise event, develops large ground deformation above the earthquake fault region in a relatively narrow zone as compared with that developed by interplate earthquakes of a comparable magnitude scale. The resulting tsunami due to this earthquake was successfully recorded by ocean bottom pressure gauges operated by the Japan Agency for Marine Earth Science and Technology (JAMSTEC), shown as MPG1 and MPG2 in Figure 10 and showed a clear dispersive tsunami waveform with first arrival of a longer-period tsunami wave and a long tail. The narrow area of large ground elevation over the source fault area and the propagation of tsunami from the source to MPG1 and 2 along the deep ($H = 4000$ m) water depth developed dispersive tsunami waveform dramatically.

4.1.1. Simulation Models

[39] The simulation domain is also shown in Figure 10 and measures 1090×768 km. J-EGG500 bathymetry data of the Japan Oceanographic Data Center was used. In addition to the actual observation points MPG1 and MPG2, the simulated waveforms were measured at the points labeled N, E, S, W, and far W. A horizontal resolution of 500 m was used in the 2-D models, whereas a characteristic horizontal element edge length of $L_c = 1$ km was used in the 3-D NS model. The DSP model with a horizontal resolution of 1 km was also tested; the difference between the results with horizontal resolutions of 500 m and 1 km was negligible. A sponge buffer zone is used for the NS model, whereas the DSP and LLW models used a perfectly matched layer method which used thinner buffer zones (20 grid points) at the edge of the computational domain [*Maeda and Furumura*, 2013]. Based on the wave dispersion analysis described above, a vertical resolution of five layers (of nodes) was used in the 3-D NS model. The number of vertical layers is the same everywhere following the topographic variations of the sea bottom, except for shallow regions. The number of vertical layers is kept to two in the regions shallower than 50 m. With these resolutions, the computational mesh in the 3-D NS model had 379,994 nodes in the horizontal plane; the whole mesh with five vertical layers had 1,822,033 nodes and 8,633,757 elements. The time step was 1.0 s in every model.

[40] As the earthquake source model, we assumed a flat fault plane with a constant slip. The epicenter was at (137.14°E, 33.14°N). The strike, dip, and rake of the fault were 135°, 40°, and 123°, respectively. The size of the fault was 60×32 km, the top depth of the fault was 2 km, and the slip on the fault was 1.29 m. For these fault parameters, we refer to *Saito and Furumura* [2009a] and Y. Yamanaka's analysis (www.eri.u-tokyo.ac.jp/sanchu/Seismo_Note/2004/EIC153.html). The initial sea surface deformation shown in Figure 11 was assumed to be same as the sea bottom deformation, which was derived from an analytical solution for an elastic half-space [*Okada*, 1985].

4.1.2. Simulation Results

[41] Contour plots of sea surface height at $t = 30$ min for all the models are shown in Figure 12. In Figure 12, only the domain excluding the sponge region of the NS model is shown. It is evident from these plots that the LLW model does not produce any dispersive waves, while both the DSP model and the NS model produce significant dispersive features
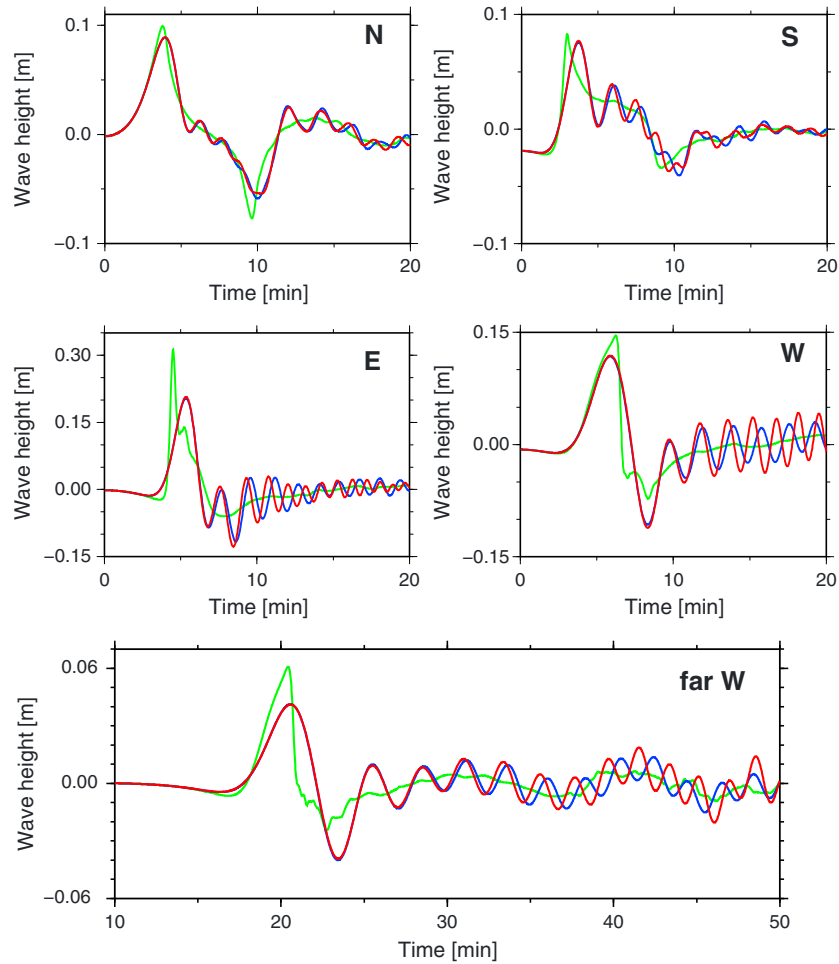
Figure 14. Waveforms of 2004 off Kii peninsula earthquake tsunami at the points N, S, E, W, and far W. Red lines are the results from the NS model, blue lines are from the DSP model, and the green lines are from the LLW model.

developed by the short wavelength tsunami propagating in the deep sea. Careful analysis of Figure 12 also shows that the dispersive tails predicted by the DSP model are stronger than those predicted by the NS model, which causes significant waves to remain near the source region in DSP model. These waves correspond to the spurious waves observed in the simple test problem shown in Figure 7.

[42] The simulated waveforms at MPG1 and MPG2 are plotted in comparison with observation in Figure 13. The observed wave height data was treated by a filtering procedure to extract the tsunami signal. In the LLW model, the initial peak is larger than that of the observation, and the dispersive features of the observed wave signal are not reproduced. In contrast, both the NS and DSP models show good agreement with observations regarding the amplitude of the initial peak, the arrival time, and the shape of the forepart of the waves. It is likely that the agreement with the observation could be improved by employing a more realistic source model, but it should be noted here that the dispersed tsunami waveforms developed by this earthquake, which propagate over a complicated bathymetry, are mostly synthesized by a proper 3-D NS simulation even using a simple rectangle source slip model.

[43] The results from the NS and DSP models show good agreement with each other until around 35 min at both

MPG1 and MPG2. After 35 min, the waves of the DSP model fall behind those of the NS model. This delay in the DSP model waves relative to the NS model waves is consistent with the results from the simple test problems described in sections 3.1 and 3.2, and hence, we expect that the NS model simulates wave dispersion more accurately.

[44] To emphasize the difference in dispersive wave features, the waveforms at the points labeled N, S, E, W, and far W are shown in Figure 14. The wave in the direction parallel to the strike of the fault plane, i.e., the points N and S, does not show strong dispersion, and the results from the NS and DSP models are in close agreement. On the other hand, the wave in the direction perpendicular to the strike of the fault plane, i.e., the points E and W, shows strong dispersion. At these points, the difference between the waveforms of the short wavelength components in the NS and DSP models is obvious.

[45] The point far W is on the same line as E and W, 180 km from W, and close to MPG1 and MPG2. Comparing the points W and far W, we found that the waveform of dispersed tsunami is elongated gradually with propagation distance, and the initial wave height is reduced more compared to the wave height derived by the LLW model that does not include such dispersive effects. While
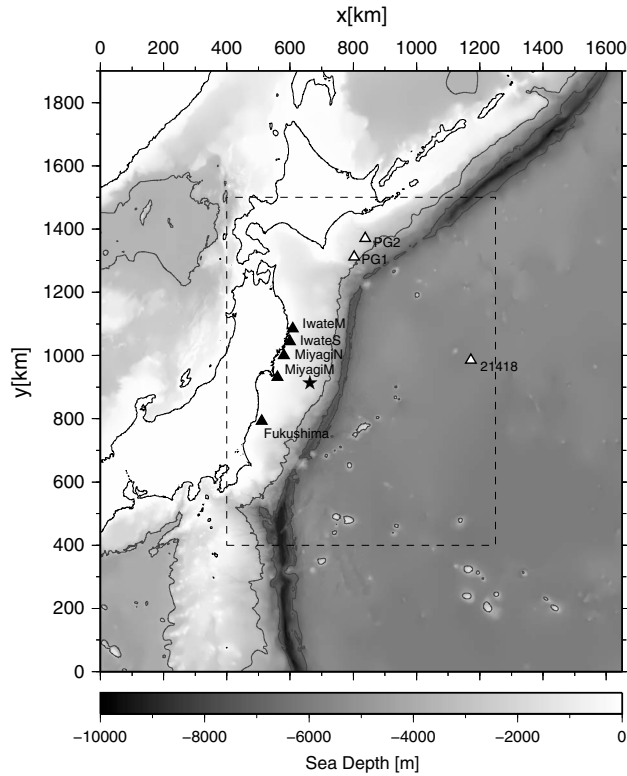
Figure 15. Bathymetry around the off Tohoku region of Japan. The locations of the ocean bottom pressure gauges, PG1, PG2, and 21418, are denoted by open triangles, and those of the GPS buoys, Iwate N, Iwate M, Iwate S, Miyagi N, Miyagi M, and Fukushima, are filled triangles. The region outside the smaller dotted line square is used for a sponge region to prevent artificial reflections at the open boundaries. The epicenter determined by Japan Meteorological Agency at 142.86°E, 38.10°N is shown by a solid star. The contour lines of the bathymetry at $H = -3500$ m and -7000 m are also shown.

the difference between the waveforms of the NS and DSP models at W becomes obvious at the third peak, the difference at far W is not obvious until the fourth or fifth peak. This is because the long wavelength components, which are more accurately predicted by the DSP model, propagate rapidly, whereas the short wavelength components, which include larger error, propagate slowly. Hence, the less accurately modeled part of the wave signal arrives later, relative to the first arrival, at large distances from the source region compared to its arrival time at small distances. As both the wave gauges used in this work were relatively far from the source, they do not provide a particularly sensitive diagnostic with which to test model performance. A better test of the DSP and NS models would be provided by wave gauge data nearer the source, where the dispersion error of the DSP model may be more obvious. We expect that the NS model would reproduce the waveforms at the points near the source more accurately than the DSP model.

4.2. 2011 Off Tohoku (M_w 9.0) Earthquake

[46] We also simulated the tsunami caused by the 2011 off Tohoku earthquake (M_w 9.0). This devastating tsunami broke over the Sanriku coast—a "Ria coast" with a complicated

structure that causes complex reflected waves. Moreover, the earthquake involved a large fault slip near the trench [e.g., *Maeda et al.*, 2011; *Fujii et al.*, 2011] that might generate a sea bottom deformation of very short wavelength. Short wavelength waves generated by such deformation are not well approximated by long wave theory and are likely to be better simulated by a 3-D NS model.

4.2.1. Simulation Models

[47] The simulated area, 1650×1900 km, is described in Figure 15. J-EGG500 bathymetry from the Japan Oceanographic Data Center and General Bathymetric Chart of the Oceans (GEBCO) from the British Oceanographic Data Centre were used. The simulated waveforms were measured at the observation points of GPS buoys (Iwate M, Iwate S, Miyagi N, Miyagi M, and Fukushima) operated by the Port and Airport Research Institute (PARI) and ocean bottom pressure gauges (PG1 and PG2 operated by JAMSTEC, the 21418 DART station by the National Oceanic and Atmospheric Administration).

[48] A characteristic horizontal mesh edge length of $L_c = 500$ m was used at the Sanriku coast, which has an especially complicated shoreline. This length was increased to 1.5 km in the open ocean and 10 km at the outmost sponge region: the mesh size was changed gradually between these regions. The horizontal mesh (511,852 nodes) is shown in Figure 1a; the whole 3-D mesh, with three layers (of nodes), had 1,505,524 nodes and 5,927,565 elements. The regions shallower than 50 m only have two layers. The time step was chosen to be 1.0 s. Here the LLW and DSP models are again applied to the same problem with 1.0 km horizontal resolution and 1.0 s time step.

[49] To represent the sea surface deformation due to this earthquake as a source of tsunami, we employed the source model proposed by *Saito et al.* [2011], derived using inversion analysis based on linear dispersive wave equations and tsunami observations from ocean bottom pressure gauges and GPS buoys. The assumed initial sea surface deformation is shown in Figure 16a, demonstrating a large area of sea surface elevation of more than 8 m in maximum near the trench and a subsidence of the sea surface of -2 m in maximum near the coast.

4.2.2. Simulation Results

[50] Contour plots of sea surface height at $t = 0$, 5, 10, and 20 min from the earthquake starts are shown in Figure 16 for the NS model with three vertical layers, and those at $t = 30$, 40, 50, and 60 min are shown in Figure 17. At $t = 5$ min, the largest amplitude initial tsunami along the trench starts propagating mainly in the east-west directions with decreasing wave height (-2.11 m $\leq \eta \leq 4.45$ m). The wave going west keeps the shape of the initial wave distribution characterized by a moderate curve in the west part and a steep curve in the east part. Then, at $t = 10$ min, large amplitude subsidence of the sea surface (-3.66 m $\leq \eta \leq 3.4$ m) appears behind the westward tsunami, which is eventually observed at Miyagi observation stations (Figure 18). At $t = 20$ min, the westward tsunami gets close to the coast with larger amplitude (-3.41 m $\leq \eta \leq 5.17$ m) and shorter wavelength. The westward tsunami still basically preserves the shape with longer wave length in the west and shorter wave length in the east, which are recorded by Iwate and Miyagi observation stations (Figure 18). At $t = 30$ min, the positive wave height tsunamis start attacking the west coast of Japan (-5.40 m $\leq \eta \leq 11.7$ m).
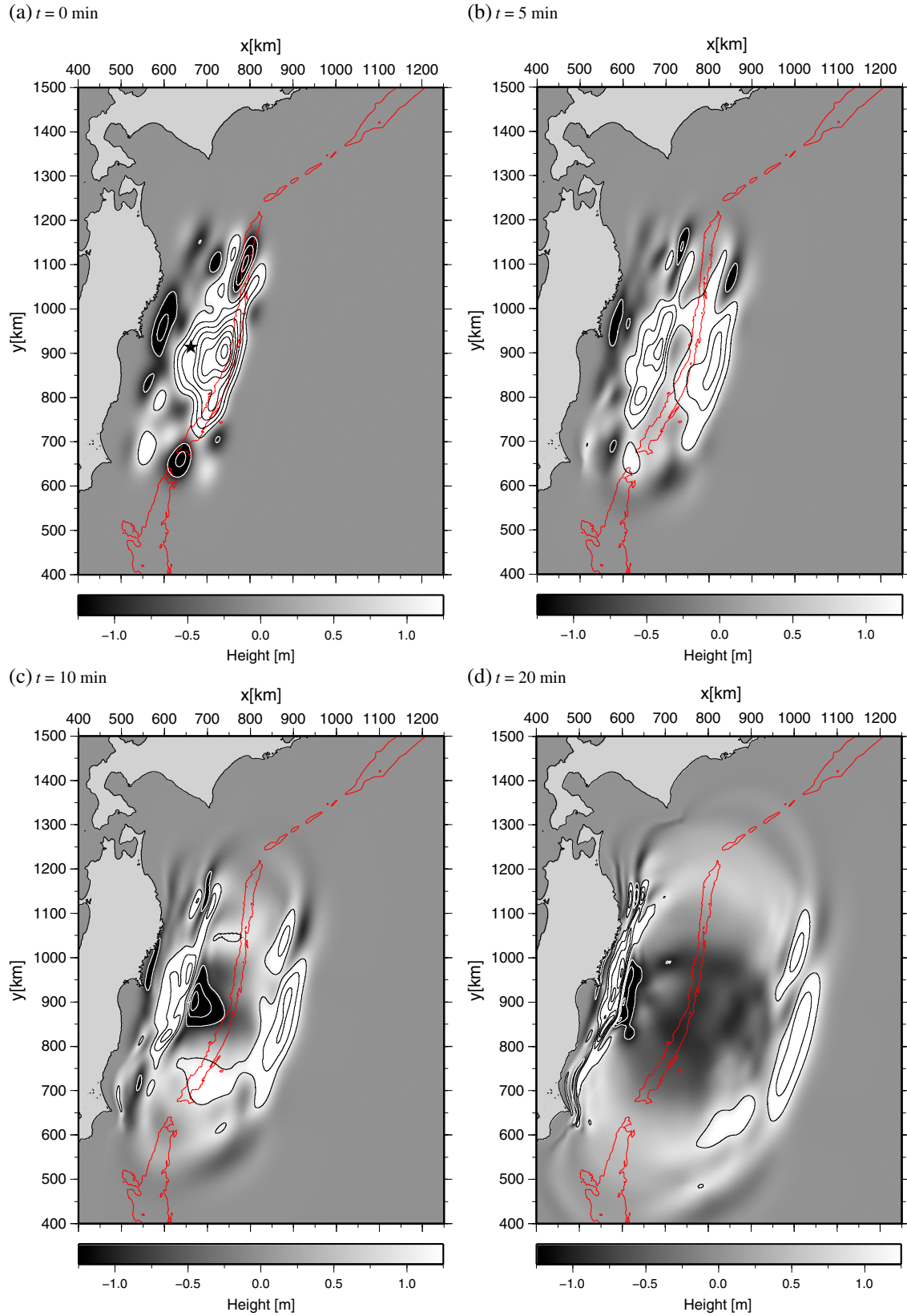
Figure 16. Snapshots of the simulations of the 2011 off Tohoku earthquake tsunami at different time steps. In Figure 16a, the epicenter determined by JMA at 142.86°E, 38.10°N is shown by a solid star. The contour lines of wave height are shown with step size of 1 m skipping the wave height of 0 m. The contour line of bathymetry at $H = 7000$ m is also shown in red.
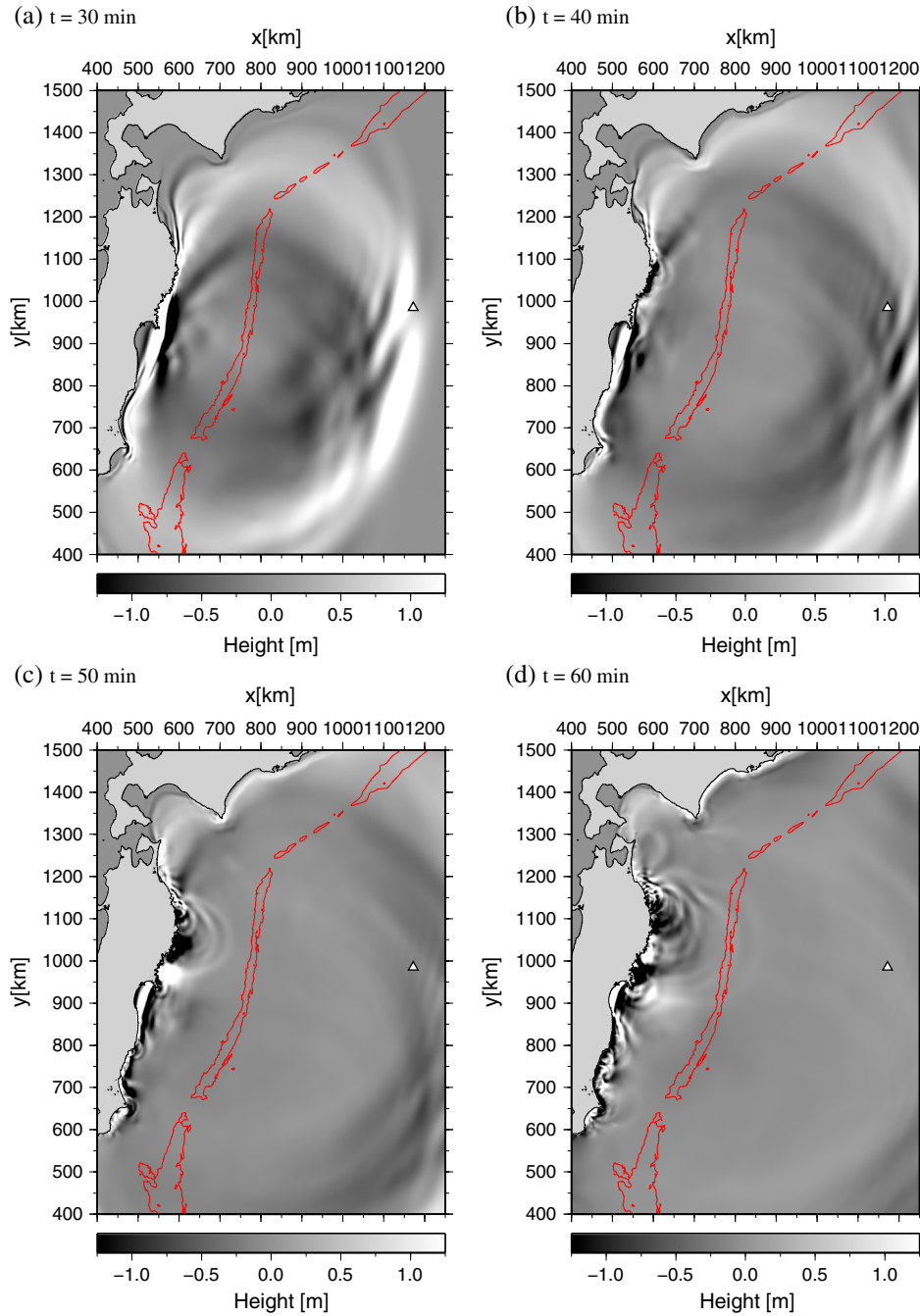
Figure 17. Snapshots of the simulation of the 2011 off Tohoku earthquake tsunami. The location of 21418 DART observation station is also shown by an open triangle. The contour line of bathymetry at $H = 7000$ m is also shown in red.

The eastward tsunami propagating in the deep ocean generates a dispersive tail behind the initial longer wavelength wave, which can be observed at the wave heading to the 21418 DART station. After $t = 40$ min, complex waves reflected at the coast continuously attack the coast dominating the wave pattern near the coastal region.

[51] The simulated waveforms are compared with the observations in Figure 18. The comparison shows good agreement between the simulation results and the observations. In the north direction, i.e., at PG1 and PG2, only a long wavelength and relatively small amplitude wave ($\eta \leq 0.6$ m) were

obtained both from the observation and the simulation. At the GPS observation stations near the coast, a long wavelength wave arrives first being followed by a short wavelength fluctuation. However, in the simulations, the maximum wave height of the short wavelength wave is not as large as the observation, which is especially clear around $t = 25$ min at Iwate M and Iwate S. This is presumably because of an underestimation of the fault slip near the trench region. At the 21418 station, the waveform after the initial peak shows significant wave dispersion that cannot be reproduced by a LLW model [*Saito et al.*, 2011]. The NS
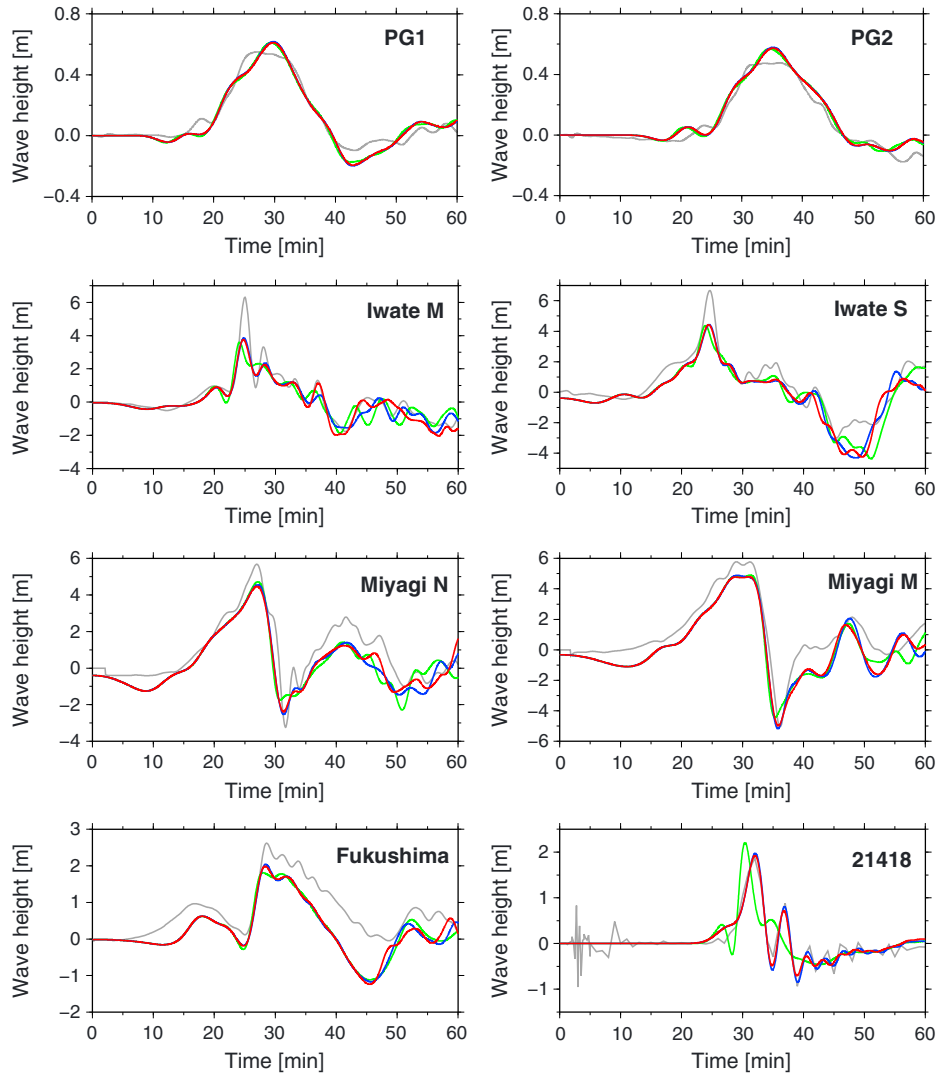
Figure 18. Waveforms of the 2011 off Tohoku earthquake tsunami at observation points. Gray lines are the observation, and red lines are the results from the NS model with three nonuniform vertical layers (of nodes). Blue and green lines are the results from the DSP and LLW models, respectively.

model successfully reproduces both the initial peak and also the second and third peaks showing its ability to accurately model wave dispersion.

[52] In Figure 18, the results from the LLW and DSP models are also shown. In the LLW model, the peak with the maximum wave height arrives slightly earlier than for the observation and for the results from the NS and DSP models at Iwate M, Iwate S, and 21418 as is expected from the discussion in section 3.2. For these stations, the wave with the maximum height is narrow compared to the other stations, where such discrepancy is not so obvious. The NS and DSP models are in relatively good agreement with observation and each other, but the discrepancies between these two models are obvious at GPS buoys after around 40 min, where the waves reflected from the coastline are observed. Comparing the NS and the DSP models, at 21418, a little phase lag is observed after around third or fourth peak of the wave. As the source model is based on inversion analysis using a similar DSP model to the present DSP model, the agreement with the observation is better in the DSP model than in the NS model.

[53] The parallel computation performance of the Tohoku tsunami simulations was measured on an Intel Xeon X5670 (2.93 GHz) and X5675 (3.07 GHz) CPU cluster. Using 256 cores, this simulation required 23 hours of CPU time (wall clock time) to evaluate tsunami over 1 h with 3600 time steps in the calculation. The results are compared to the corresponding ideal performance (perfect parallel scaling) in Figure 19. On the basis of simulation performance on 64 cores, the parallel efficiency on 512 cores is 92.6%. The corresponding performance of the DSP model, with a horizontal resolution of 750 m (2 times higher than the NS model) and the same time step of 1 s, was measured on an Intel X3480 CPU (3.07 GHz) workstation (Figure 19). When a large number (~1024) of CPU cores are employed and the performance of the code scales ideally, the computation time of the 3-D NS model becomes similar to that of a DSP model performed on a single processor. Note that the DSP model tested here is linear, and a nonlinear version would require a longer computation time.
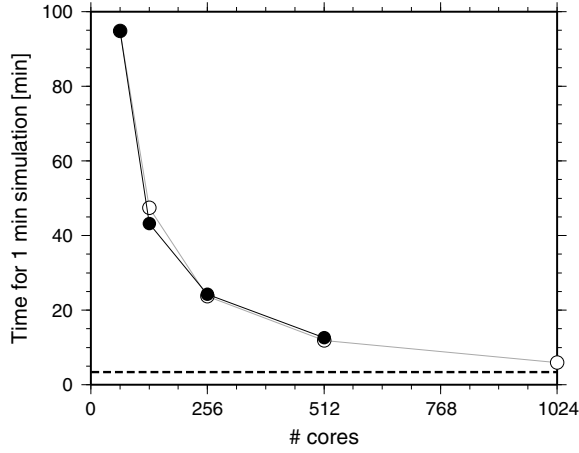
Figure 19. Computation time to simulate 1 min of the 2011 off Tohoku earthquake tsunami. Filled circles and open circles are the measured timings and the ideal parallel performance based on the timing on 64 cores, respectively. The computation time of the DSP model on one core is also shown by a dotted line.

5. Discussion and Conclusions

[54] This paper describes the simulations of tsunami propagation in a large domain using a parallel 3-D NS model that employs an unstructured mesh finite element method using the Fluidity-ICOM code.

[55] Compared to the tsunami simulation based on conventional 2-D LLW model, our 3-D NS model accurately accounts for tsunami wave dispersion, and thus, the amplitude and arrival time of the first wave peak. On the other hand, the peak of tsunami is usually higher and arrives earlier in the LLW model.

[56] Although the model developed here is 3-D, the vertical resolution is limited, which minimizes the computational cost. By comparing the ability of linear DSP models and the NS model to simulate wave dispersion, it was found that an NS model with three or five vertical layers (of nodes) achieves greater accuracy than general DSP models, especially regarding the wave velocity of short wavelength components. Also, unlike DSP models, the dispersion characteristics can be improved dramatically by simply increasing the vertical resolution.

[57] Simulations of tsunamis generated by the off Kii peninsula earthquake tsunami of 2004 showed the effectiveness of our 3-D NS model as compared with the 2-D DSP models to simulate dispersive tsunami waveform in the near-source region. These differences between tsunami waveform derived by NS and DSP simulations were particularly noticeable in the direction perpendicular to the strike of the fault plane and were not as obvious in the direction parallel to the fault strike or at observation points far from the source. This is because the shorter wavelength components, for which the DSP model is not as accurate, tend to be produced in the across strike direction, travel slowly, and arrive late at points far from the source.

[58] In an effort to capture tsunami signals at locations near the source, the Dense Ocean floor Network System for Earthquakes and Tsunamis (DONET) of JAMSTEC recently began to record dense observations of sea surface height using ocean bottom pressure gauges in the off Kii peninsula region [*Kaneda*, 2010]. The studies with the GPS buoys for tsunami observation relocated farther from the coast are also ongoing. To precisely reproduce such near-source, high-resolution observations which capture source-rupture processes directly is becoming more important, and in this endeavor, the 3-D NS model may contribute well.

[59] The main drawback of the 3-D model is the computational cost, which was overcome in this work using parallel computing. In the off Tohoku earthquake case, the computation time of our present 3-D NS simulation using about 1000 CPU cores could be of comparable speed to a 2-D linear dispersive wave model running on a single CPU core, assuming a good parallel scalability of the code. As the current world fastest-class supercomputers, such as the K computer which has 0.7 million CPU cores and achieved more than 10 petaflops (http://www.top500.org), become more widespread, we believe high accuracy 3-D tsunami simulations will become more tractable.

[60] In future extensions of this study, the tsunami inundation process will be investigated using the 3-D NS model to model the reflection of tsunamis more accurately and to assess the hazard to life and property. A wetting and drying algorithm was recently implemented in Fluidity-ICOM [*Funke et al.*, 2011], and it is expected that unstructured meshes will allow multiscale, high-resolution inundation simulations using high-resolution topography data to be used in seamless combination with propagation simulations in the open ocean using comparatively low-resolution bathymetry data.

Appendix A: Discretization

[61] In this appendix, we will briefly review the details of the discretization method used in Fluidity-ICOM for the runs performed in this paper. The discretization is based on a mixed continuous/discontinuous Galerkin finite element method using the so-called $P_{1,DG}P_2$ finite element pair for velocity and pressure. This discretization is advantageous for ocean applications [*Cotter et al.*, 2009a, 2009b] due to its exact representation of geostrophic balance, and its LBB stability, thus avoiding the need for pressure stabilization, typically required in standard, equal order finite element methods. Pressure stabilization generally leads to excessive damping of waves.

[62] We will start by considering a standard continuous Galerkin discretization of the incompressible Navier-Stokes equations (4) and (2). The first step is to write the equations in weak form, i.e.,

$$\int_{\Omega} \mathbf{v}\frac{\partial \mathbf{u}}{\partial t} + \mathbf{v}\cdot(\mathbf{u}\cdot\nabla\mathbf{u}) + \mathbf{v}\cdot\nabla\frac{p}{\rho_0} - \mathbf{v}\cdot\nu\nabla^2\mathbf{u} = 0, \qquad (A1)$$

$$\int_{\Omega} q\nabla\cdot\mathbf{u} = 0 \qquad (A2)$$

for all vector functions $\mathbf{v} \in V$ and scalar functions $q \in W$ in some adequately chosen test spaces V and W [e.g., *Gresho et al.*, 1984]. The 3-D domain that is integrated over is denoted by Ω. Integration by parts of the viscosity term in the momentum equation, and the divergence term in the continuity equation gives

$$\int_\Omega \mathbf{v} \frac{\partial \mathbf{u}}{\partial t} + \mathbf{v}\cdot(\mathbf{u}\cdot\nabla\mathbf{u}) + \mathbf{v}\cdot\nabla\frac{p}{\rho_0} - \nu(\nabla\mathbf{v}) : (\nabla\mathbf{u}) + \int_\Gamma \nu\mathbf{v}\cdot(\mathbf{n}\cdot\nabla\mathbf{u}) = 0, \tag{A3}$$

$$-\int_\Omega \nabla q\cdot\mathbf{u} + \int_\Gamma q\mathbf{n}\cdot\mathbf{u} = 0, \tag{A4}$$

where $\mathbf{n}$ denotes the unit outward normal vector to the boundary Γ. The extra boundary terms can be used to implement weak boundary conditions. At the ocean bottom and coastlines, we substitute equation (7) to weakly enforce a no-normal flow and free-slip condition (no bottom drag or wind forcing is considered here). Similarly, we can substitute an expression for $\mathbf{n}\cdot\mathbf{u}$ obtained from equation (6) at the free surface. Thus, we obtain

$$\int_\Omega \mathbf{v} \frac{\partial \mathbf{u}}{\partial t} + \mathbf{v}\cdot(\mathbf{u}\cdot\nabla\mathbf{u}) + \mathbf{v}\cdot\nabla\frac{p}{\rho_0} - \nu(\nabla\mathbf{v}) : (\nabla\mathbf{u}) = 0, \tag{A5}$$

$$-\int_\Omega \nabla q\cdot\mathbf{u} + \int_{\Gamma\text{fs}} q\frac{\mathbf{n}_{\text{fs}}\cdot\mathbf{e}_z}{\rho_0 g}\frac{\partial p}{\partial t} = 0, \tag{A6}$$

where $\mathbf{n}_{\text{fs}}$ denotes the normal vector to the free surface boundary Γ_{fs}. The finite element discretization of these continuous equations in weak form now proceeds by restricting the solutions $\mathbf{u}$ and p, and the test functions $\mathbf{v}$ and q, to finite-dimensional trial and test spaces. For the continuous Galerkin (CG) method, $\mathbf{u}$ and $\mathbf{v}$ are chosen from the same test and trial space V_h, and similarly, p and q are restricted to the same test and trial space W_h. A typical way to obtain such finite-dimensional function spaces is to consider a computational mesh of triangular (in 2-D), or tetrahedral (in 3-D) elements, and to restrict the function space to all piecewise polynomials of a certain degree. For the CG method, we have the additional restriction that the functions should be continuous between elements.

[63] If the functions $\{\mathbf{N}_i\} \in V_h$ and $\{M_i\} \in W_h$ are sets of basis functions for V_h and W_h, respectively, we may write

$$\mathbf{u}(\mathbf{x}) = \sum_i u_i\mathbf{N}_i(\mathbf{x}), \mathbf{v}(\mathbf{x}) = \sum_i v_i\mathbf{N}_i(\mathbf{x}), \tag{A7}$$

$$p(\mathbf{x}) = \sum_i p_i M_i(\mathbf{x}), q(\mathbf{x}) = \sum_i q_i M_i(\mathbf{x}), \tag{A8}$$

where u_i, v_i, p_i, and q_i are coefficients that determine $\mathbf{u}$, $\mathbf{v}$, p, and q as linear combinations of the basis functions. Substituting these expressions into (A5) and (A6), we can write the discretized equations as the following two compact matrix equations:

$$\mathbf{M}\frac{d}{dt}\underline{\mathbf{u}} + \mathbf{A}(\mathbf{u}) + \frac{1}{\rho_0}\mathbf{G}\underline{p} + \mathbf{K}\underline{\mathbf{u}} = 0, \tag{A9}$$

$$-\mathbf{G}^T\underline{\mathbf{u}} + \mathbf{M}_{\text{fs}}\frac{\mathrm{d}}{\mathrm{d}t}\underline{p} = 0, \tag{A10}$$

where $\underline{\mathbf{u}}$ and $\underline{p}$ are vectors formed by the coefficients u_i and p_i, and the coefficients of the mass matrix $\mathbf{M}$, (nonlinear) advection matrix $\mathbf{A}(\mathbf{u})$, gradient matrix $\mathbf{G}$, viscosity matrix $\mathbf{K}$, and free surface mass matrix $\mathbf{M}_{\text{fs}}$ are given by

$$\mathbf{M}_{ij} = \int_\Omega \mathbf{N}_i\cdot\mathbf{N}_j, \tag{A11}$$

$$\mathbf{A}(\mathbf{u})_{ij} = \int_\Omega \mathbf{N}_i\cdot(\mathbf{u}\cdot\nabla\mathbf{N}_j), \tag{A12}$$

$$\mathbf{G}_{ij} = \int_\Omega \mathbf{N}_i\cdot\nabla M_j, \tag{A13}$$

$$\mathbf{K}_{ij} = \int_\Omega \nu(\nabla\mathbf{N}_i) : (\nabla\mathbf{N}_j), \tag{A14}$$

$$\mathbf{M}_{\text{fs},ij} = \int_{\Gamma\text{fs}} \frac{\mathbf{n}_{\text{fs}}\cdot\mathbf{e}_\mathbf{z}}{\rho_0 g}M_i M_j. \tag{A15}$$

[64] Note that we may omit the coefficients v_i and q_i of the test functions as the equations should hold for every test function $\mathbf{v} \in V_h$ and $q \in W_h$. The matrix associated with the divergence term in the continuity equation is equal to the transpose of the discrete gradient matrix.

[65] In discontinuous Galerkin (DG) methods, the test and trial functions spaces are extended to include functions that are discontinuous between elements. The above derivation, however, cannot be applied directly as derivatives are not defined at the jump in the solution across the element boundaries. Additional integrals over the element boundaries have to be introduced to deal with these. For the momentum advection term this is achieved via a standard discontinuous Galerkin discretization [e.g., *Hesthaven and Warburton*, 2008]. The viscosity term is discretized using the so-called compact discontinuous Galerkin method [*Peraire and Persson*, 2008]. In the $P_{1,DG}P_2$ mixed discretization, we only allow for discontinuities in the velocity solution. The velocity solution space $V_h = P_{1,DG}$ consists of all piecewise linear functions, whereas for the pressure solution, only continuous, piecewise quadratic functions are considered ($W_h = P_2$). Since the pressure gradient term and the divergence term only involve derivatives of continuous functions $M_j \in P_2$, no additional interelement integral terms are required here. The distribution of degrees of freedom in the $P_{1,DG}P_2$ mixed discretization is illustrated in Figure A1.

[66] To satisfy incompressibility of the flow at each time step, a pressure correction method [e.g., *Gresho et al.*, 1984] is employed. A nonlinear iteration scheme (Picard iteration) is also employed to deal with the nonlinear advection term, and nonlinear iterations are done within a time step.

[67] At the first step, a preliminary velocity field $\underline{\mathbf{u}}_*^{n+1}$ is obtained by solving the discretized momentum equation,

$$\mathbf{M}\frac{\underline{\mathbf{u}}_*^{n+1} - \underline{\mathbf{u}}^n}{\Delta t} + \mathbf{A}(\widetilde{\mathbf{u}})\cdot\underline{\mathbf{u}}_*^{n+1/2} + \frac{1}{\rho_0}\mathbf{G}\widetilde{\underline{p}}^{n+1/2} + \mathbf{K}\underline{\mathbf{u}}_*^{n+1/2} = 0, \tag{A16}$$

where $\underline{\mathbf{u}}_*^{n+1/2} = (\underline{\mathbf{u}}_*^{n+1} + \underline{\mathbf{u}}^n)/2$ and $\widetilde{\underline{p}}^{n+1/2} = (\widetilde{\underline{p}} + \underline{p}^n)/2$. The values $\widetilde{\underline{u}}$ and $\widetilde{\underline{p}}$ are our current best estimates of the velocity and pressure at the end of the time step. In the first nonlinear iteration, these start as $\widetilde{\underline{u}} = \underline{\mathbf{u}}^n$ and $\widetilde{\underline{p}} = \underline{p}^n$, but will be updated in the next iteration using the $\underline{\mathbf{u}}^{n+1}$ and $\underline{p}^{n+1}$ obtained in the first iteration. For the time integration, the Crank-Nicolson scheme is employed here. The continuity

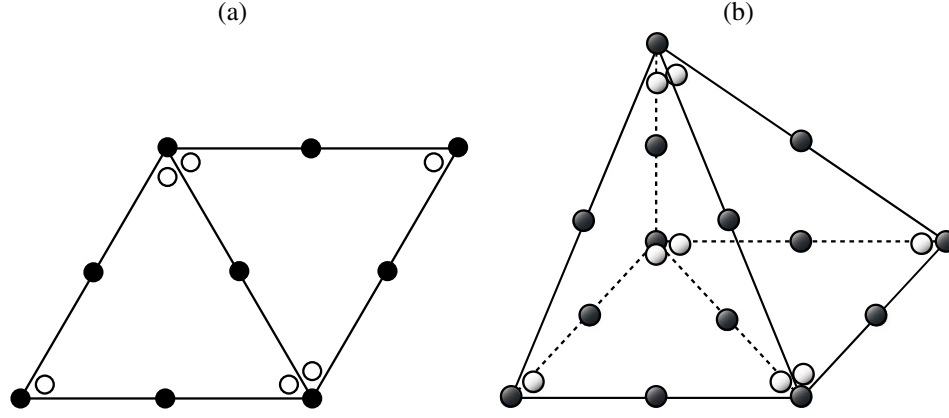(a)   (b)

Figure A1. Distribution of the degrees of freedom in the 2-D triangle and 3-D tetrahedron $P_{1,\text{DG}}P_2$ elements. The neighboring two elements are shown. (a) 2-D element with filled circles of the continuous quadratic pressure nodes and open circles of the discontinuous linear velocity nodes. (b) 3-D element with black spheres representing pressure nodes and white spheres representing velocity nodes.

equation, with the divergence term evaluated at the $(n+1/2)$-th time step, can also be written in the matrix form

$$-\mathbf{G}^T\underline{\mathbf{u}}^{n+1/2} + \frac{\mathbf{M}_{fs}}{\Delta t}\left(\underline{\mathbf{p}}^{n+1} - \underline{\mathbf{p}}^n\right) = 0, \qquad (A17)$$

where $\underline{\mathbf{u}}^{n+1/2} = \left(\underline{\mathbf{u}}^{n+1} + \underline{\mathbf{u}}^n\right)/2$. In the present method, pressure and velocity are updated via the following equations

$$\underline{\mathbf{p}}^{n+1} = \widetilde{\underline{\mathbf{p}}} + \Delta\underline{\mathbf{p}}, \qquad (A18)$$

$$\underline{\mathbf{u}}^{n+1} = \underline{\mathbf{u}}_*^{n+1} - \frac{\Delta t}{2\rho_0}\mathbf{M}^{-1}\mathbf{G}\Delta\underline{\mathbf{p}}. \qquad (A19)$$

[68] The pressure correction Δp is constructed such that pressure and velocity satisfy the continuity equation. By multiplying (A19) by $\mathbf{G}^T$ and substituting it and (A18) into the continuity equation (A17), we have a discrete Poisson equation called the pressure correction equation

$$\left(\frac{\Delta t}{4\rho_0}\mathbf{G}^T\mathbf{M}^{-1}\mathbf{G} + \frac{\mathbf{M}_{fs}}{\Delta t}\right)\Delta\underline{\mathbf{p}} = \mathbf{G}^T\underline{\mathbf{u}}_*^{n+1/2} - \frac{\mathbf{M}_{fs}}{\Delta t}\left(\widetilde{\underline{\mathbf{p}}} - \underline{\mathbf{p}}^n\right). \quad (A20)$$

[69] The pressure correction $\Delta\underline{\mathbf{p}}$ is obtained by solving (A20). As a nonlinear advection term is included, this procedure is iterated within a time step. Here two iterations are employed. In the second step of the nonlinear iteration, the advective velocity $\widetilde{u}$ and the pressure $\widetilde{p}$ of (A16) are updated by $\underline{\mathbf{u}}^{n+1}$ and $\underline{\mathbf{p}}^{n+1}$ obtained in the first nonlinear iteration. The variables $\underline{\mathbf{u}}^{n+1}$ and $\underline{\mathbf{p}}^{n+1}$ are then treated as unknowns and are solved for again.

[70] The procedure in one time step can be summarized as

[71] Step 1: Assume $\widetilde{u} = \mathbf{u}^n$ and $\widetilde{p} = \underline{\mathbf{p}}^n$ in the discrete momentum equation (A16).

[72] Step 2: Solve (A16) for the intermediate velocity $\underline{\mathbf{u}}_*^{n+1}$.

[73] Step 3: Solve the discrete Poisson equation (A20) for the pressure correction $\Delta\underline{\mathbf{p}}$.

[74] Step 4: Update the pressure $\underline{\mathbf{p}}^{n+1}$ using (A18).

[75] Step 5: Update the velocity $\underline{\mathbf{u}}^{n+1}$ using (A19).

[76] Step 6: Update $\widetilde{u}$ and $\widetilde{p}$ in (A16) with the $\underline{\mathbf{u}}^{n+1}$ and $\underline{\mathbf{p}}^{n+1}$ obtained in Steps 4 and 5.

[77] Step 7: Repeat Steps 2–5 to yield the final $\underline{\mathbf{u}}^{n+1}$ and $\underline{\mathbf{p}}^{n+1}$.

[78] To solve the discrete momentum equation (A16), a successive over-relaxation (SOR) preconditioned generalized minimal residual (GMRES) method is used. For the Poisson equation (A20), the conjugate gradient method is used with an algebraic multigrid method as a preconditioner [*Kramer et al.*, 2010].

[79] Further details of the discretization methods used in Fluidity-ICOM and references to papers that they are based on can be found in the Fluidity-ICOM manual (http://amcg. ese.ic.ac.uk/fluidity). The model, including its source code, can be downloaded freely from http://launchpad.net/fluidity.

Appendix B: 2-D Linear Long Wave and Dispersive Wave Models

[80] To verify the ability of the present 3-D NS model to simulate tsunamis and clarify its advantages or drawbacks compared to the conventional approaches, two kinds of conventional 2-D wave models are employed in this paper, one based on linear long wave (LLW) equations and one based on linear dispersive wave (DSP) equations.

[81] When the 3-D NS equations are integrated in the vertical direction with the kinematic boundary condition (5) at the sea surface and the no-normal flow condition at the sea bottom assuming that the fluid is inviscid and irrotational, the pressure at the free surface is zero, the wave height is small comparing to the sea depth, $\eta \ll H$, and the vertical acceleration of a water particle is much smaller than the gravity acceleration, the linear long wave equations are obtained

$$\frac{\partial M}{\partial t} + gh\frac{\partial \eta}{\partial x} = 0$$
$$\frac{\partial N}{\partial t} + gh\frac{\partial \eta}{\partial y} = 0 \quad, \qquad (B1)$$
$$\frac{\partial \eta}{\partial x} = -\frac{\partial M}{\partial x} - \frac{\partial N}{\partial y}$$

where M and N are the horizontal velocities integrated

vertically from the sea bottom to the sea surface. The numerical algorithm in the LLW model is based on the popular conventional approach with finite difference discretization with an orthogonal staggered mesh and a leapfrog time integration scheme. Because of the leapfrog scheme, η is defined at $t = n\Delta t$, and M and N are defined at $t = (n + 1/2)\Delta t$ where n is a time step and Δt is the time step interval. For the open boundaries, we employ a perfectly matched layer algorithm [*Maeda and Furumura*, 2013].

[82] For the DSP model, we employ the following equations [e.g., *Saito et al.*, 2010],

$$
\begin{aligned}
\frac{\partial M}{\partial t} + gh\frac{\partial \eta}{\partial x} &= \left[\frac{1}{3}h^2\frac{\partial^2}{\partial x\partial t}\left(\frac{\partial M}{\partial x} + \frac{\partial N}{\partial y}\right)\right] \\
\frac{\partial N}{\partial t} + gh\frac{\partial \eta}{\partial y} &= \left[\frac{1}{3}h^2\frac{\partial^2}{\partial y\partial t}\left(\frac{\partial M}{\partial x} + \frac{\partial N}{\partial y}\right)\right], \\
\frac{\partial \eta}{\partial x} &= -\frac{\partial M}{\partial x} - \frac{\partial N}{\partial y}
\end{aligned} \tag{B2}
$$

in which a dispersive term has been added to equation (B1). The same spatial discretization scheme as the LLW model is used. For the time integration, a leapfrog implicit time integration scheme is used in which η is defined at $t = n\Delta t$ and M and N are defined at $t = (n + 1/2)\Delta t$. To update M and N, linear simultaneous equations obtained by discretizing equation (B2) are solved by the Gauss-Seidel iteration method. This causes the computation time of the DSP model to be large compared to the LLW model. The present DSP model was developed with reference to *Saito et al*. [2010]. The open boundaries are dealt with as for the LLW model.

Appendix C: Analytical Solution for Wave Propagation

[83] Analytical solutions for wave generation and propagation processes were formulated for incompressible and irrotational flow with a constant sea depth [e.g., *Takahashi*, 1942]. *Saito and Furumura* [2009b] refer to this theory as linear potential theory and formulated this assuming a finite rise time in Cartesian coordinates. Here we assume that the deformation occurs instantaneously; i.e., the rise time is zero. When the vertical displacement of the sea bottom is d(x,y), the sea surface height at each position is described as

$$
\begin{aligned}
\eta(x,y,t) &= \frac{\partial \xi}{\partial t} \\
&= \frac{1}{(2\pi)^2}\int_{-\infty}^{\infty}\int_{-\infty}^{\infty} d\mathbf{k}\exp(i\mathbf{k}\cdot\mathbf{x})\cos\gamma t\frac{1}{\cosh kH}\hat{d}(\mathbf{k})\, \text{for}\ t\geq 0,
\end{aligned} \tag{C1}
$$

where

$$
\xi(x,y,t) = \frac{1}{(2\pi)^2}\int_{-\infty}^{\infty}\int_{-\infty}^{\infty} d\mathbf{k}\exp(i\mathbf{k}\cdot\mathbf{x})\frac{\sin\gamma t}{\gamma}\frac{1}{\cosh kH}\hat{d}(\mathbf{k}), \tag{C2}
$$

$$
\gamma = k\sqrt{gH}\sqrt{\frac{1}{kH}\tanh kH}, \tag{C3}
$$

and

$$
\hat{d}(\mathbf{k}) = \frac{1}{(2\pi)^2}\int_{-\infty}^{\infty}\int_{-\infty}^{\infty} d\mathbf{x}d(x,y)\exp(-i\mathbf{k}\cdot\mathbf{x}). \tag{C4}
$$

Appendix D: Free-Slip and No-Slip Bottom Boundary Conditions

[84] In this paper, we employed a free-slip boundary condition at the bottom to avoid resolving the thin boundary layer that appears when applying a no-slip condition. While a free-slip boundary condition is a simplification of the flow near the seafloor, its use makes it possible to achieve excellent accuracy with only three to five vertical layers. Here we compare results using free-slip and no-slip bottom boundary conditions to show how this assumption affects wave propagation. The majority of the NS models described in this paper were in 3-D, but in this section (and section 3.1), 2-D vertical slice NS models with the same equations and discretization as the 3-D models were employed to test higher vertical resolution cases.

[85] To generate a wave, a perturbation is added at the sea bottom as $d(x, t = 0) = d_0\exp(-x^2/a^2)$ with a characteristic length scale of $a = 2.5$ km and an amplitude of $d_0 = 1.0$ m. The sea depth is set to $H = 4000$ m. Assuming instantaneous deformation of the seafloor, analytical solutions of the initial sea surface deformation and the subsequent wave propagation were calculated using equation (C1). The analytical solution for the initial sea surface deformation was used as the initial condition in the following simulations.

[86] Snapshots of the wave height at $t = 600$ s are shown in Figure D1, where the horizontal resolution and the time step are fixed to 200 m and 1.0 s, respectively, and different vertical resolutions are tested. Here uniform, structured (in the vertical and horizontal) meshes are used in both free-slip and no-slip cases. The free-slip cases with more than three vertical layers showed good agreement with the analytical solution, and the results from the cases with more than two vertical layers overlap each other in Figure D1a. On the other hand, the no-slip cases do not agree well with the analytical solution except for the highest vertical resolution case with 41 vertical layers.

[87] A vertical cross section at $t = 600$ s from the free-slip case with 41 vertical layers, for which wave height agreed very well with the analytical solution, is shown in Figure D2. To investigate the effect of the bottom boundary condition on the flow structure, velocity, and pressure profiles with depth at the initial wave peak are shown in Figure D3. In each case, this peak is located around $x = 100$–110 km. As we described in section A, pressure has three degrees of freedom per element edge. Therefore, for example, there are five data points in the vertical direction for the case of three layers of mesh nodes (two layers of elements). As for velocity, multiple values are related to one mesh node because of its discontinuity, and the median value is shown in Figure D3. In the no-slip cases, a boundary layer can be seen at the bottom of the horizontal velocity curve, which requires high resolution at the bottom to resolve. When the vertical resolution is increased and the boundary layer is well-resolved, the pressure- and velocity-depth profile of the no-slip case converges to that of the high-resolution free-slip case with 41 vertical layers. And, as shown in
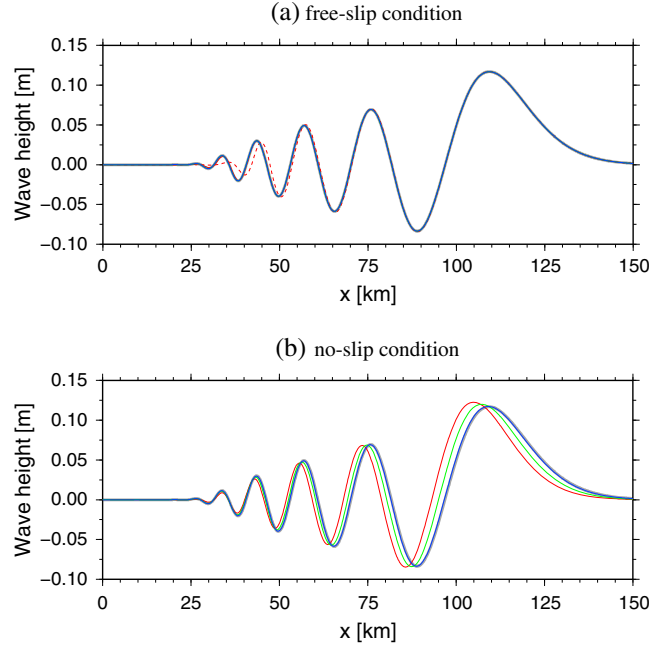
Figure D1. Snapshots of wave height at $t = 600\,\mathrm{s}$ for the cases with (a) free-slip and (b) no-slip boundary conditions at the bottom. The analytical solution is in gray. The results from 3, 5, and 41 vertical layers cases are denoted by red, green, and blue solid lines, respectively. The result from two-layer case is shown only in the free-slip case by a red dashed line.

Figure D1, the wave height (i.e., pressure perturbation at the sea surface) converges to the analytical solution. On the other hand, in Figure D3, the free-slip case with only three vertical layers gives a closer vertical depth profile to the free-slip 41-layer case when compared to the no-slip cases in which the three layer profile is noticeably different from the corresponding no-slip 41-layer case. The free-slip pressure-depth profiles show especially good agreement which results in good agreement on the wave height (Figure D1). We can conclude that the free-slip case with low vertical resolution gives a similar wave propagation to the no-slip case with higher vertical resolution when the ocean depth is large.

Appendix E: Horizontal Resolution

[88] To investigate the importance of the horizontal resolution in representing the short wavelength dispersive wave, different horizontal resolution cases are tested here. The problem setup was the same as described in section D. The number of vertical layers and the time step were set to three and 1.0 s, respectively, in all cases. Horizontal resolutions of $\Delta x = 200$, 400, 2000, and 5000 m were tested. The results are compared with the analytical solution in Figure E1. The case of $\Delta x = 5000\,\mathrm{m}$ agreed with the analytical solution up to the third peak and that of $\Delta x = 2000\,\mathrm{m}$ agreed up to the sixth peak. Overall, the waveform diverges from the analytical solution
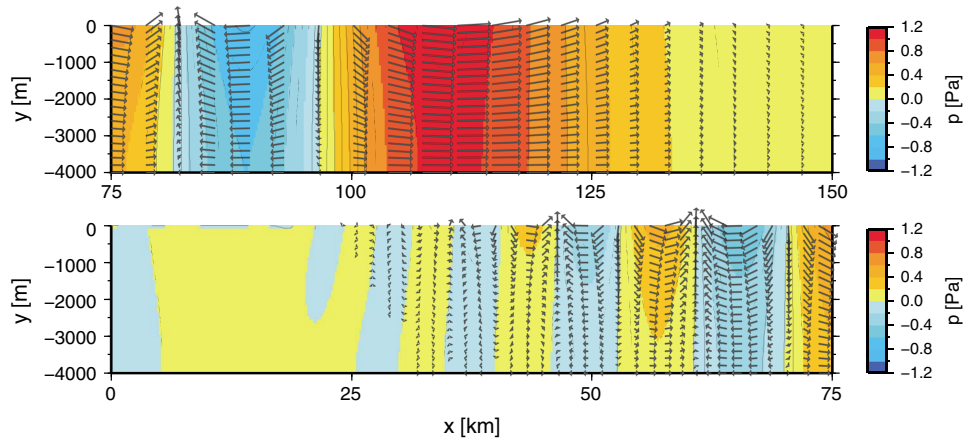

Figure D2. Snapshots at $t = 600\,\mathrm{s}$ of the case with free-slip and 41 vertical layers. The contour denotes the pressure perturbation. The increment in the contour lines is 0.1. The arrows illustrate the velocities.
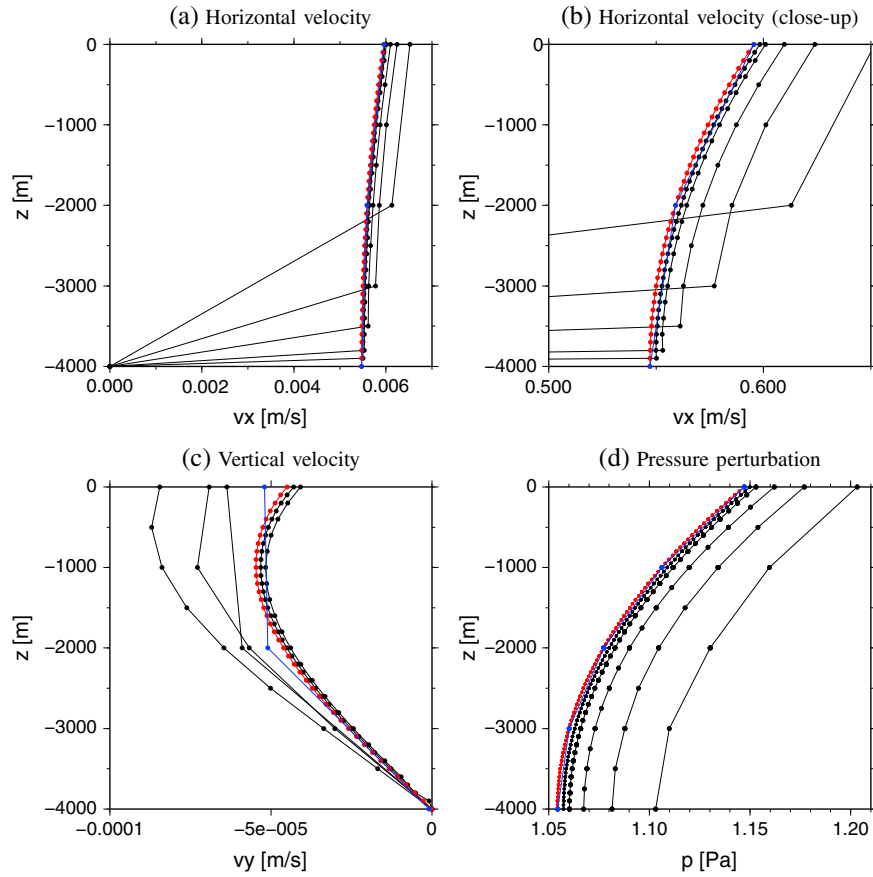
(a) Horizontal velocity

(b) Horizontal velocity (close-up)

(c) Vertical velocity

(d) Pressure perturbation

Figure D3. Horizontal velocity, vertical velocity and pressure as a function of depth beneath the initial wave peak at $t = 600$ s. A value at each node is plotted as a filled circle. The results from the no-slip cases with five different vertical resolutions of 3, 5, 9, 21, and 41 layers are shown in black, and the result from the free-slip case with 3 and 41 vertical layers are in blue and red, respectively.

(a) $\Delta x = 5000$ and 2000 m
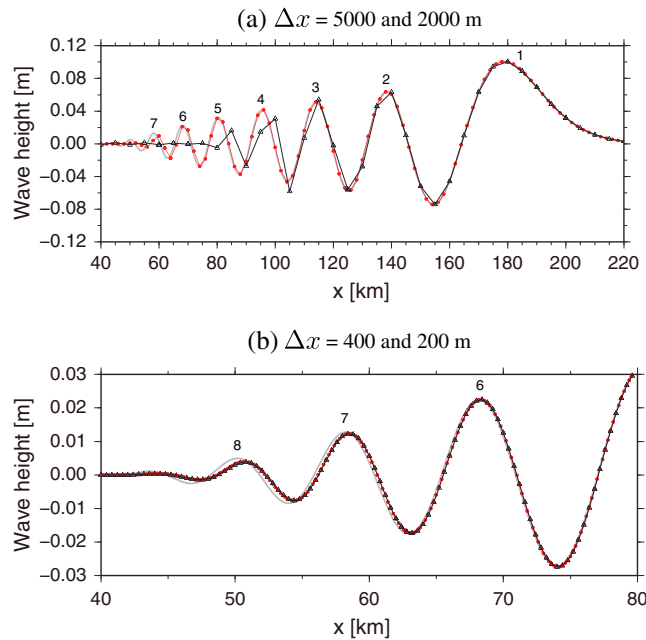
(b) $\Delta x = 400$ and 200 m

Figure E1. Same as Figure D1 with free-slip condition for $t = 960$ s. (a) $\Delta x = 5000$ and 2000 m are shown in black and red, respectively. (b) $\Delta x = 400$ and 200 m are shown in black and red, respectively. In both Figures 1a and 1b, the analytical solution is shown in gray with the wave peaks numbered.

when the number of horizontal computational nodes within half a wavelength is less than three. The case with horizontal resolutions of 200 and 400 m showed good agreement with the analytical solution up to the sixth or seventh peak. After that, the dispersion error became significant.

References

Abadie, S., D. Morichon, S. Grilli, and S. Glockner (2010), Numerical simulation of waves generated by landslides using a multiple-fluid Navier-Stokes model, *Coastal Engineering*, 57, 779–794, doi:10.1016/j.coastaleng.2010.03.003.

Ai, C., S. Jin, and B. Lv (2010), A new fully non-hydrostatic 3-D free surface flow model for water wave motions, *Int. J. Numer. Methods Fluids*, 66(11), 1354–1370, doi:10.1002/fld.2317.

Beji, S., and K. Nadaoka (1996), A formal derivation and numerical modelling of the improved Boussinesq equations for varying depth, *Ocean Eng.*, 23(8), 691–704, doi:10.1016/0029-8018(96)84408-8.

Castro, C. E., M. Käser, and E. F. Toro (2009), Space-time adaptive numerical methods for geophysical applications, *Philos. Trans. R. Soc. A*, 367(1907), 4613–4631, doi:10.1098/rsta.2009.0158.

Cerjan, C., D. Kosloff, R. Kosloff, and M. Reshef (1985), A nonreflecting boundary condition for discrete acoustic and elastic wave equations, *Geophysics*, 50(4), 705–708, doi:10.1190/1.1441945.

Cotter, C. J., D. A. Ham, and C. C. Pain (2009a), A mixed discontinuous/continuous finite element pair for shallow-water ocean modelling, *Ocean Modell.*, 26(1–2), 86–90, doi:10.1016/j.ocemod.2008.09.002.

Cotter, C. J., D. A. Ham, C. C. Pain, and S. Reich (2009b), LBB stability of a mixed Galerkin finite element pair for fluid flow simulations, *J. Comput. Phys.*, 228(2), 336–348, doi:10.1016/j.jcp.2008.09.014.

Fujii, Y., K. Satake, S. Sakai, M. Shinohara, and T. Kanazawa (2011), Tsunami source of the 2011 off the Pacific coast of Tohoku, Japan earthquake, *Earth Planets Space*, 63, 815–820, doi:10.5047/eps.2011.06.010.

Funke, S. W., C. C. Pain, S. C. Kramer, and M. D. Piggott (2011), A wetting and drying algorithm with a combined pressure/free-surface formulation for non-hydrostatic models, *Adv. Water Resour.*, 34(11), 1483–1495, doi:10.1016/j.advwatres.2011.08.007.

Gresho, P. M., S. T. Chan, R. L. Lee, and C. D. Upson (1984), A modified finite element method for solving the time-dependent, incompressible Navier-Stokes equations, Part 2: Applications, *Int. J. Numer. Methods Fluids*, 4(7), 619–640, doi:10.1002/fld.1650040703.

Guesmia, M., P. Heinrich, and C. Mariotti (1998), Numerical simulation of the 1969 Portuguese tsunami by a finite element method, *Nat. Hazards*, 17(1), 31–46, doi:10.1023/A:1007920617540.

Hesthaven, J. S., and T. Warburton (2008), *Nodal Discontinuous Galerkin Methods*, Texts in Applied Mathematics vol. 54, p. 16, Springer, New York, doi:10.1007/978-0-387-72067-8.

Kaneda, Y. (2010), The advanced ocean floor real time monitoring system for mega thrust earthquakes and tsunamis-application of DONET and DONET2 data to seismological research and disaster mitigation, in *OCEANS 2010*, pp. 1–6.

Kawahara, M., T. Kodama, and M. Kinoshita (1988), Finite element method for tsunami wave propagation analysis considering the open boundary condition, *Comput. Math. Appl.*, 16(1–2), 139–152, doi:10.1016/0898-1221(88)90028-4.

Kramer, S. C., C. J. Cotter, and C. C. Pain (2010), Solving the Poisson equation on small aspect ratio domains using unstructured meshes, *Ocean Modell.*, 35(3), 253–263, doi:10.1016/j.ocemod.2010.08.001.

Madsen, P. A., and O. R. Sørensen (1992), A new form of the Boussinesq equations with improved linear dispersion characteristics. Part 2. A slowly-varying bathymetry, *Coastal Eng.*, 18(3–4), 183–204, doi:10.1016/0378-3839(92)90019-Q.

Maeda, T., and T. Furumura (2013), FDM simulation of seismic waves, ocean acoustic waves, and tsunamis based on tsunami-coupled equations of motion, *Pure Appl. Geophys.*, 170(1–2), 109–127, doi:10.1007/s00024-011-0430-z.

Maeda, T., T. Furumura, S. Sakai, and M. Shinohara (2011), Significant tsunami observed at the ocean-bottom pressure gauges at 2011 off the Pacific coast of Tohoku earthquake, *Earth Planets Space*, 63, 803–808, doi:10.5047/eps.2011.06.005.

Mitsotakis, D. E. (2009), Boussinesq systems in two space dimensions over a variable bottom for the generation and propagation of tsunami waves, *Math. Comput. Simul.*, 80(4), 860–873, doi:10.1016/j.matcom.2009.08.029.

Myers, E. P., and A. M. Baptista (1995), Finite element modeling of the July 12, 1993 Hokkaido Nansei-Oki tsunami, *Pure Appl. Geophys.*, 144(3), 769–801, doi:10.1007/BF00874394.

Nwogu, O. (1993), Alternative form of Boussinesq equations for nearshore wave propagation, *J. Waterw. Port Coastal Ocean Eng.*, 119(6), 618–638, doi:10.1061/(ASCE)0733-950X(1993)119:6(618.

Okada, Y. (1985), Surface deformation due to shear and tensile faults in a half-space, *Bull. Seismol. Soc. Am.*, 75(4), 1135–1154.

Peraire, J., and P. O. Persson (2008), The compact discontinuous Galerkin (CDG) method for elliptic problems, *SIAM J. Sci. Comput.*, 30(4), 1806–1824, doi:10.1137/070685518.

Peregrine, D. H. (1967), Long waves on a beach, *J. Fluid Mech.*, 27(04), 815–827, doi:10.1017/S0022112067002605.

Piggott, M. D., G. J. Gorman, C. C. Pain, P. A. Allison, A. S. Candy, B. T. Martin, and M. R. Wells (2008), A new computational framework for multi-scale ocean modelling based on adapting unstructured meshes, *Int. J. Numer. Methods Fluids*, 56(8), 1003–1015, doi:10.1002/fld.1663.

Saito, T., and T. Furumura (2009a), Three-dimensional simulation of tsunami generation and propagation: Application to intraplate events, *J. Geophys. Res.*, 114, B02307, doi:10.1029/2007JB005523.

Saito, T., and T. Furumura (2009b), Three-dimensional tsunami generation simulation due to sea-bottom deformation and its interpretation based on the linear theory, *Geophys. J. Int.*, 178(2), 877–888, doi:10.1111/j.1365-246X.2009.04206.x.

Saito, T., K. Satake, and T. Furumura (2010), Tsunami waveform inversion including dispersive waves: The 2004 earthquake off Kii Peninsula, Japan, *J. Geophys. Res.*, 115, B06303, doi:10.1029/2009JB006884.

Saito, T., Y. Ito, D. Inazu, and R. Hino (2011), Tsunami source of the 2011 Tohoku-Oki earthquake, Japan: Inversion analysis based on dispersive tsunami simulations, *Geophys. Res. Lett.*, 38, L00G19, doi:10.1029/2011GL049089.

Takahashi, R. (1942), On seismic sea waves caused by deformations of the sea bottom (in Japanese with English abstract), *Bull. Earthquake Res. Inst. Univ. Tokyo*, 41, 545–571.

Tanioka, Y., K. Satake, and L. Ruff (1995), Total analysis of the 1993 Hokkaido Nansei-Oki Earthquake using seismic wave, tsunami, and geodetic data, *Geophys. Res. Lett.*, 22(1), 9–12, doi:10.1029/94GL02787.

Walters, R. A. (2005), A semi-implicit finite element model for non-hydrostatic (dispersive) surface waves, *Int. J. Numer. Methods Fluids*, 49(7), 721–737, doi:10.1002/fld.1019.

Xiao, H., and W. Huang (2008), Numerical modeling of wave runup and forces on an idealized beachfront house, *Ocean Engineering*, 35(1), 106–116, doi:10.1016/j.oceaneng.2007.07.009.